






ARTICLE

Mechanosensitive calcium flashes promote sustained RhoA activation during tight junction remodeling

Saranyaraajan Varadarajan¹ , Shahana A. Chumki² , Rachel E. Stephenson¹, Eileen R. Misterovich¹, Jessica L. Wu¹, Claire E. Dudley¹ , Ivan S. Erofeev³, Andrew B. Goryachev³ , and Ann L. Miller^{1,2} 

Epithelial cell–cell junctions remodel in response to mechanical stimuli to maintain barrier function. Previously, we found that local leaks in tight junctions (TJs) are rapidly repaired by local, transient RhoA activation, termed “Rho flares,” but how Rho flares are regulated is unknown. Here, we discovered that intracellular calcium flashes and junction elongation are early events in the Rho flare pathway. Both laser-induced and naturally occurring TJ breaks lead to local calcium flashes at the site of leaks. Additionally, junction elongation induced by optogenetics increases Rho flare frequency, suggesting that Rho flares are mechanically triggered. Depletion of intracellular calcium or inhibition of mechanosensitive calcium channels (MSCs) reduces the amplitude of calcium flashes and diminishes the sustained activation of Rho flares. MSC-dependent calcium influx is necessary to maintain global barrier function by regulating reinforcement of local TJ proteins via junction contraction. In all, we uncovered a novel role for MSC-dependent calcium flashes in TJ remodeling, allowing epithelial cells to repair local leaks induced by mechanical stimuli.

Introduction

The ability of epithelial tissues to establish and maintain a selective paracellular barrier is crucial for development of multicellular organisms and proper function of vital organs (Ivanov et al., 2010; Luissint et al., 2016; Marchiando et al., 2010; Moriwaki et al., 2007). The dynamic nature of epithelial tissues during development and organ homeostasis requires cells to change shape and remodel their cell–cell junctions during cell- and tissue-generated forces including cell division, cell extrusion, and intercalation (Gudipaty and Rosenblatt, 2016; Guillot and Lecuit, 2013; Varadarajan et al., 2019). Remarkably, epithelia are able to maintain barrier function despite these shape-change events (Higashi et al., 2016; Rosenblatt et al., 2001; Stephenson et al., 2019). However, the mechanisms by which epithelial cells remodel their cell–cell junctions without compromising barrier function are not fully understood.

In vertebrates, epithelial barrier function is regulated by the apical junctional complex, including tight junctions (TJs) and adherens junctions (AJs; Zihni et al., 2016). Claudins and Occludin, which are both transmembrane TJ proteins, interact with their counterparts on neighboring cells and polymerize within the membrane to form a network of TJ strands that selectively regulate the passage of small ions and macromolecules between the cells (Claude and Goodenough, 1973; Furuse et al., 1998;

Staehein et al., 1969). TJ strands are connected to the underlying actomyosin array by the zonula occludens (ZO) family of scaffolding proteins, thereby coupling barrier function to actomyosin-mediated cell shape changes (Fanning et al., 1998; Furuse et al., 1998; Itoh et al., 1999; Van Itallie et al., 2017). Although it is known that mechanical stress leads to a global increase in permeability to macromolecules (Cavanaugh et al., 2006; Cohen et al., 2008; Samak et al., 2010), much less is known about how cells respond to these leaks.

We recently reported the occurrence of short-lived leaks associated with cell-generated mechanical forces in the developing *Xenopus laevis* epithelium (Stephenson et al., 2019). During *Xenopus* gastrulation, the epithelial monolayer covering the animal cap of the developing embryo undergoes frequent cell divisions and morphogenetic movements, requiring elongation of cell–cell junctions to accommodate cell shape changes. Leaks are associated with elongating junctions and happen at sites where TJ proteins are locally reduced. Leaks are dynamically repaired by localized, short-lived activations of the small GTPase RhoA, which we termed “Rho flares” (Stephenson et al., 2019). Rho flares are also associated with local membrane protrusion at the site of leaks. Together, the correlation of Rho flares with junction elongation and membrane

¹Department of Molecular, Cellular, and Developmental Biology, University of Michigan, Ann Arbor, MI; ²Cellular and Molecular Biology Program, University of Michigan, Ann Arbor, MI; ³Centre for Synthetic and Systems Biology, University of Edinburgh, Edinburgh, Scotland.

Correspondence to Ann L. Miller: annlm@umich.edu.

© 2022 Varadarajan et al. This article is distributed under the terms of an Attribution–Noncommercial–Share Alike–No Mirror Sites license for the first six months after the publication date (see <http://www.rupress.org/terms/>). After six months it is available under a Creative Commons License (Attribution–Noncommercial–Share Alike 4.0 International license, as described at <https://creativecommons.org/licenses/by-nc-sa/4.0/>).

curvature suggest that RhoA may be activated by a mechanosensitive pathway.

Calcium signaling plays a key role in transducing mechanical forces into biochemical signals during cell shape changes (Christodoulou and Skourides, 2015; Sahu et al., 2017). Calcium signaling varies from long-range calcium waves to subcellular calcium transients, both of which are controlled precisely in space and time to modulate cytoskeleton-mediated cell shape changes. Calcium signaling is associated with local RhoA activation during mechanical events including wound healing (Benink and Bement, 2005; Clark et al., 2009), cell migration (Pardo-Pastor et al., 2018), and dendritic spine enlargement (Murakoshi et al., 2011), suggesting the possibility of calcium-mediated RhoA activation during TJ remodeling.

Elevation of intracellular calcium following a mechanical stimulus can be mediated by influx of extracellular calcium through mechanosensitive calcium channels (MSCs) in the plasma membrane (PM) or calcium release from the ER (Shao et al., 2015). PM localized MSCs, including the piezo and transient receptor potential (TRP) ion channel families, allow calcium influx in response to local and/or global changes in membrane tension or curvature (Coste et al., 2010; Gudipaty et al., 2017; Liu and Montell, 2015; Miyamoto et al., 2014; Mochizuki et al., 2009; Shi et al., 2018). For example, during cell migration, MSCs mediate transient calcium influx at lamellipodia and focal adhesions to guide the direction of migration (Ellefsen et al., 2019; Wei et al., 2009). However, the role of MSCs in force-dependent remodeling of TJs has not been explored.

Here, we investigate the mechanism by which Rho flares are activated during TJ remodeling using high-resolution live imaging of the gastrula-stage *Xenopus* epithelium, optogenetics, laser-induced TJ injury, and a microscopy-based barrier assay. We discover that local intracellular calcium flashes are a consequence of paracellular leaks that happen in response to junction elongation. Using optogenetics, we show that junction elongation is a mechanical stimulus that induces Rho flares. Further, we demonstrate that intracellular calcium flashes, which are dependent on MSCs but not inositol 1,4,5-trisphosphate receptors (IP₃Rs), support the Rho flare-mediated TJ repair pathway. Finally, we show that MSC-mediated calcium flashes regulate local junction contraction through robust, sustained Rho activation to maintain an intact barrier.

Results

Epithelial barrier leaks induce a local intracellular calcium increase

Intracellular calcium signaling has been implicated in TJ biogenesis, establishment of barrier function, and actomyosin-mediated cell shape changes (Christodoulou and Skourides, 2015; Gonzalez-Mariscal et al., 1990; Nigam et al., 1992; Suzuki et al., 2017). Thus, we hypothesized that intracellular calcium signaling might be involved in Rho flare-mediated TJ repair of local barrier leaks. To test this idea, we performed zinc-based ultrasensitive microscopic barrier assay (ZnUMBA; Stephenson et al., 2019) in gastrula-stage (Nieuwkoop and Faber stage

10.5–12) *Xenopus* embryos expressing probes for intracellular calcium (tagBFP-C2; modified from Yu and Bement [2007]) and active Rho (mCherry-2xrGBD; Benink and Bement, 2005; Davenport et al., 2016). The C2 domain of PKC β , when bound to calcium, is recruited from the cytoplasm to the PM and is capable of detecting both local and global calcium increases. High-speed live imaging demonstrated that calcium increases locally at leak sites (Fig. 1 A). FluoZin-3 intensity increased, indicating a leak, before the local calcium increase at the site of the Rho flare (Fig. 1 B), and FluoZin-3 intensity returned to baseline after the increase in calcium and active Rho, indicating restoration of barrier function (Fig. 1 B and Video 1).

To evaluate the spatial origin of the calcium increase at Rho flares, we generated kymographs at the site of Rho flares. A representative kymograph shows that the intracellular calcium increase originates at the junctional PM and spreads asymmetrically into the adjacent cells (Fig. 1 C). Of note, the asymmetric calcium increase is mirrored by a similar asymmetric increase in active Rho intensity in each of the cells adjacent to the PM (Fig. 1, C and D; and Video 2).

Because Rho flares precede TJ reinforcement (Stephenson et al., 2019), we next examined whether the local calcium increase precedes ZO-1 reinforcement. Indeed, time-lapse imaging of the TJ protein ZO-1 with probes for calcium (mNeon-C2) and active Rho (mCherry-2xrGBD), revealed that the local calcium increase precedes ZO-1 reinforcement (Fig. 1 D). Together, these results show that a local calcium increase originates at sites of TJ leaks and is followed by ZO-1 reinforcement.

Intracellular calcium flashes precede Rho flares during local ZO-1 reinforcement

To better characterize the temporal dynamics of the intracellular calcium increase, we used GCaMP6m (Chen et al., 2013), a genetically encoded calcium probe with faster kinetics but reduced spatial sensitivity compared with the C2 calcium probe. We detected a transient increase in calcium in cells adjacent to junctions with Rho flares (Fig. 2 A) with a duration of 74.50 ± 9.901 s (Fig. 2 B), hereafter referred to as a “calcium flash.” Calcium flashes associated with Rho flares differ from calcium waves previously described during *Xenopus* gastrulation in that calcium flashes are restricted to the cells adjacent to the junction exhibiting a Rho flare (Fig. S1, A and B; and Video 3). In contrast, calcium waves originate in two to four cells and propagate to neighboring cells within minutes (Wallingford et al., 2001; Fig. S1, C–C'; and Video 3).

When detected with GCaMP6m, calcium flashes occur after the decrease in ZO-1, and the peak of the calcium flash precedes the peak of Rho flares by ~ 80 s (Fig. 2, C and D). Further, the intensity of GCaMP6m decreases as reinstatement of ZO-1 initiates (Fig. 2 D and Video 4). As both Rho flares and calcium flashes vary in amplitude from cell to cell, we hypothesized that there is relationship between the intensity of calcium flashes and Rho flares. Correlation analysis comparing the intensity of active Rho with the intensity of calcium flashes for individual Rho flares revealed a strong positive correlation between calcium intensity and active Rho intensity (Pearson's correlation coefficient, $r = 0.7247$; Fig. S1 F). Taken together, our results

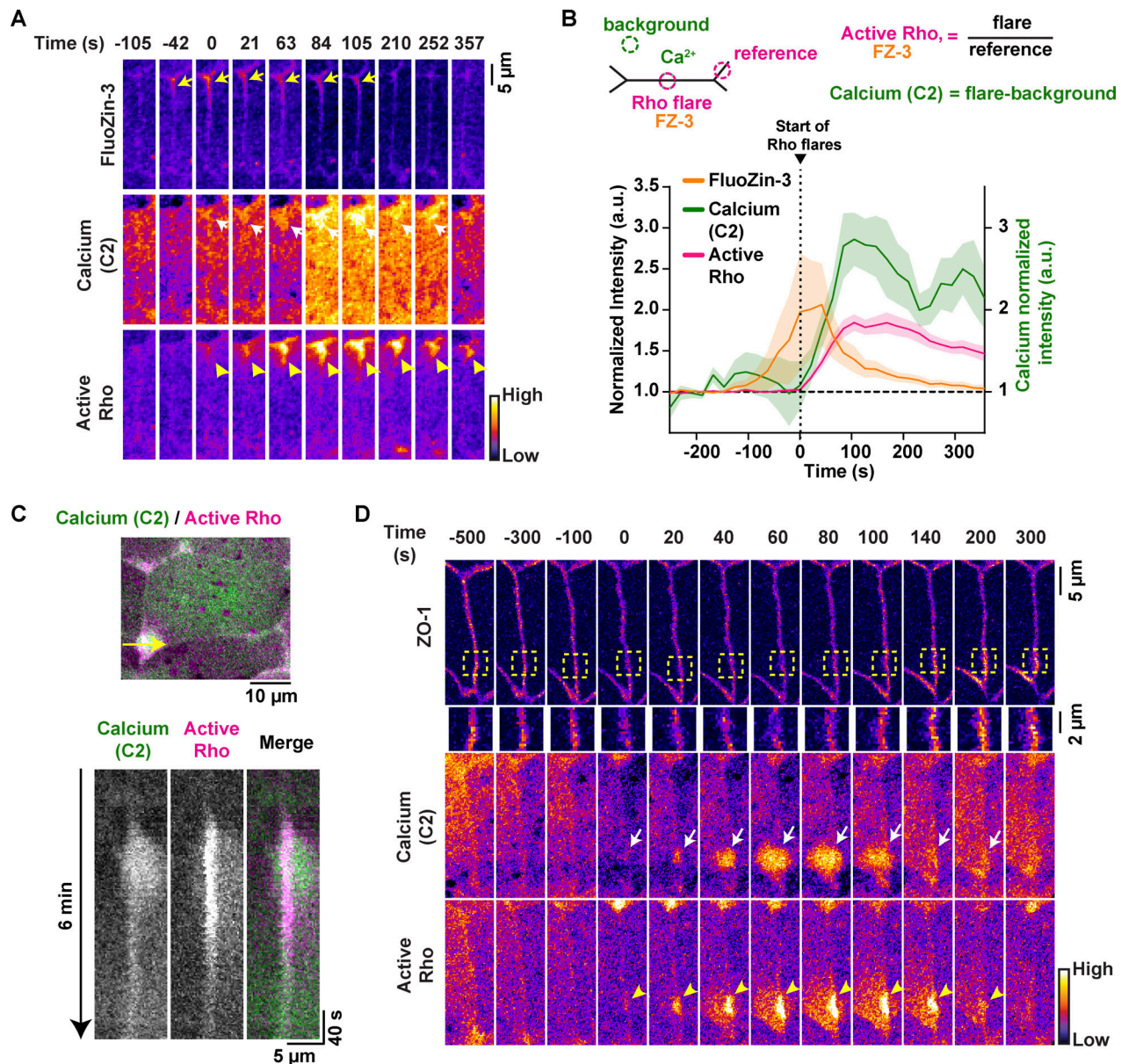


Figure 1. Epithelial paracellular leaks induce a local intracellular calcium increase. (A) Time-lapse images (Fire LUT) of FluoZin-3 dye, membrane calcium probe (tagBFP-PKC β-C2), and active Rho (mCherry-2xrGBD). Calcium increase (white arrows) follows a paracellular leak indicated by increase in FluoZin-3 fluorescence (yellow arrows) at the site of Rho flare (yellow arrowheads). Time 0 s represents start of Rho flare. (B) Quantification of experiments shown in A. Top: Schematic showing ROIs used to quantify Rho flares, calcium (C2), and FluoZin-3. Bottom: Graph of mean normalized intensity shows that the leak (FluoZin-3) precedes the increases in local calcium and active Rho. Shaded region represents SEM; n = 18 flares, 10 embryos, 6 experiments. (C) Top: Cell view of an embryo expressing membrane calcium probe (mNeon-PKCβ-C2, green) and active Rho probe (mCherry-2xrGBD, magenta). The yellow arrow indicates the 5-pixel-wide region used to generate the kymograph. Bottom: Kymograph shows that calcium increase originates at the junction and then spreads. (D) Time-lapse images (FIRE LUT) of BFP-ZO-1, membrane calcium probe (mNeon-PKC β-C2), and active Rho (mCherry-2xrGBD). Local calcium increase (white arrows) is spatially localized to the site of ZO-1 decrease (yellow boxed region) and Rho flare (yellow arrowheads).

support a role for calcium flashes in promoting Rho flare-mediated TJ reinforcement.

Next, we tested if we could recapitulate calcium flashes by experimentally inducing barrier leaks. To test this, we used 405 nm light to locally injure the TJ in cells expressing probes for F-actin (Lifeact-GFP) and cytosolic calcium (R-GECO1). We have previously shown that laser injury of the TJ causes a leak in the barrier that is repaired similarly to naturally occurring Rho flares (Stephenson et al., 2019). A fluorescent probe that strongly

localizes to the junction is necessary to induce a laser injury. Because F-actin and active RhoA increase nearly simultaneously following TJ leaks (Stephenson et al., 2019), we used Lifeact-GFP to facilitate efficient injury as well as monitor the Rho-mediated repair dynamics.

Upon laser injury, calcium increased locally at the site of the injury, followed by an F-actin increase at the site of the injury (Fig. 2, E and F; and Video 5), and the peak of calcium preceded the peak of F-actin by ~52 s (Fig. 2 F), comparable to naturally

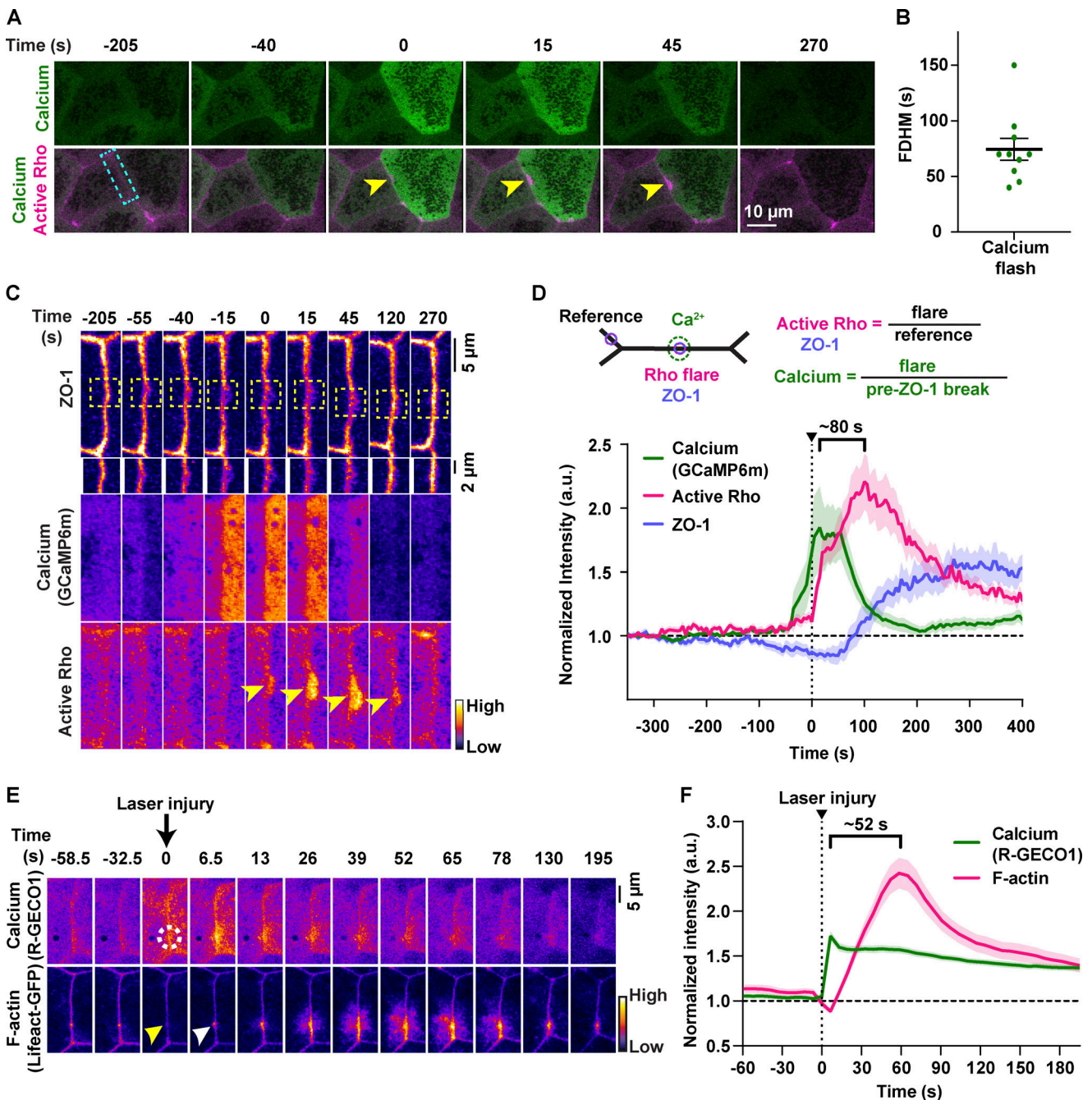


Figure 2. **Intracellular calcium flashes precede Rho flares during local ZO-1 reinforcement.** (A) Time-lapse images of calcium (GCaMP6m, green) and active Rho (mCherry-2xrGBD, magenta). Calcium flash occurs in cells adjacent to the junction with the Rho flare (yellow arrowheads). Time 0 s represents start of Rho flare. (B) Dot plot of calcium flash duration (full duration at half-maximum, FDHM). Error bars represent mean \pm SEM; $n = 10$ calcium flashes, 10 embryos, 9 experiments. (C) Montage of the junction indicated by the blue box in A (FIRE LUT). A calcium flash (GCaMP6m) follows a local loss of ZO-1 (BFP-ZO-1, yellow boxed region, enlarged below) and precedes the Rho flare (mCherry-2xrGBD, yellow arrowheads). (D) Quantification of experiments shown in C. Top: Schematic showing ROIs used to quantify Rho flares, calcium (GCaMP6m), and ZO-1. Bottom: Graph showing that calcium intensity increase follows a decrease in ZO-1 and precedes an increase in active Rho. Bracket represents the time interval between the peak of calcium and active Rho. Shaded region represents SEM; $n = 19$ flares, 14 embryos, 11 experiments. (E) Time-lapse images (FIRE LUT) of calcium probe (R-GECO1) and F-actin probe (Lifect-GFP) during laser-induced TJ injury. Local calcium increase (white dotted circle) precedes F-actin increase (white arrowhead) at the site of junctional laser injury (yellow arrowhead). Time 0 s represents time of junctional injury. (F) Quantification of experiments shown in E. Graph of mean normalized intensity shows that calcium increase follows the laser-induced junctional injury (vertical dotted line) and precedes an increase in F-actin at the site of junctional injury. Bracket represents the time interval between the peak of calcium and F-actin. Shaded region represents SEM; $n = 35$ flares, 15 embryos, 3 experiments.

occurring flares (Fig. 2 D). Moreover, when cells exhibited a short calcium spike that was not sustained, F-actin did not accumulate, resulting in failure to repair the F-actin break induced by laser injury (Fig. S1, F and G'). Together, these data show that laser-induced TJ leaks result in local, sustained calcium flashes that precede F-actin accumulation, similar to naturally occurring barrier leaks.

Optogenetic activation of junctional RhoA is not sufficient for local calcium increase

Our results demonstrate that the increases in calcium and active RhoA during naturally occurring TJ remodeling are tightly coupled in space and time, with the calcium flash preceding the peak of Rho activation. A recent study showed that optogenetically controlled broad activation of RhoA leads to an increase in intracellular calcium in epithelial cells (Inaba et al., 2021). Therefore, we asked if local activation of RhoA at apical junctions is sufficient to induce a local calcium increase. To test this, we adopted the TULIP optogenetic system (Oakes et al., 2017; Strickland et al., 2012) for use in *Xenopus* to activate RhoA with high spatiotemporal resolution. The TULIP system consists of a photosensitive LOVpep domain anchored to the membrane and a photo-recruitable guanine nucleotide exchange factor (prGEF, DH domain of the RhoGEF LARG fused to tandem PDZ domains) that activates RhoA upon illumination with 405-nm light (Fig. 3 A; Wagner and Glotzer, 2016). In gastrula-stage *Xenopus* epithelia, whole-field light stimulation rapidly recruits prGEF-mCherry from the cytoplasm to the PM (Fig. S2, A and B; and Video 6). Further, optogenetic recruitment of prGEF promotes reversible activation of RhoA and whole-field tissue contractility (Fig. S2, C and D; and Video 6). Additionally, light stimulation of a single cell-cell junction results in reversible, site-specific recruitment of prGEF-mCherry (Fig. S2 E). These results demonstrate that the TULIP optogenetic system can activate RhoA and modulate contractility with high spatiotemporal specificity in *Xenopus* embryos.

We next used this system to test if optogenetic activation of RhoA at apical junctions can induce a local calcium flash. RhoA was optogenetically activated in cells expressing a probe for active RhoA (mCherry-2xrGBD) or a probe for membrane calcium (Halo-tagged C2). Light stimulation of a single junction from vertex to vertex resulted in RhoA activation at the junction within ~60 s following the start of stimulation (Fig. 3, B and C; and Video 7). Notably, intracellular calcium did not increase upon optogenetic activation of RhoA (Fig. 3, B and C'; and Video 7). Laser injury of the same junction, however, did result in a local calcium increase (Fig. 3 D and Video 7), confirming that the stimulated cells did indeed express a functional calcium probe. Together, these data demonstrate that optogenetic junctional activation of RhoA is not sufficient to induce a local calcium increase.

Intracellular calcium flash is required for Rho flare activation and ZO-1 reinforcement

Calcium is required for Rho activation during local cell shape changes including epithelial wound healing, cell migration, and dendritic spine enlargement (Clark et al., 2009; Murakoshi et al.,

2011; Pardo-Pastor et al., 2018). However, whether calcium is required for local Rho activation and ZO-1 reinforcement at TJ leaks remains unknown. To test this question, we chelated intracellular calcium using 1,2-bis(2-aminophenoxy)ethane-*N,N,N',N'*-tetraacetic acid tetrakis(acetoxymethyl ester) (BAPTA-AM), a cell-permeable calcium chelator that chelates intracellular calcium without disrupting calcium-dependent cadherin adhesion. Treatment with BAPTA-AM led to an increase in the frequency of calcium waves (Fig. S3 A), which disrupted our ability to observe calcium flashes. Calcium waves are dependent on an ER-mediated calcium release (Wallingford et al., 2001), so we blocked waves using the IP₃R blocker 2-aminoethoxydiphenyl borate (2-APB), in addition to chelating intracellular calcium with BAPTA-AM (Fig. 4 A). Upon treatment with BAPTA-AM + 2-APB (Fig. 4 A'), the intensity of calcium flashes was reduced compared with vehicle (DMSO) controls (Fig. 4, B–D and D'; and Video 8). We noted that the frequency of Rho flares was not significantly changed in BAPTA-AM + 2-APB-treated embryos (Fig. S3 B). However, active Rho was significantly reduced at sites of ZO-1 loss when intracellular calcium was chelated (Fig. 4, B, C, E, and E'; and Video 8). Additionally, ZO-1 breaks were more severe, lasted longer, and failed to be reinstated in intracellular calcium chelated embryos compared with vehicle controls (Fig. 4, B, C, F, and F'; and Video 8). Together, our results suggest that intracellular calcium increase is required for robust activation of Rho flares and efficient ZO-1 reinforcement.

Based on our results that the IP₃R blocker, 2-APB, in conjunction with calcium chelator, significantly decreases intracellular calcium flashes associated with TJ remodeling (Fig. 4), as well as evidence that ER-mediated calcium release is important for TJ biogenesis (Denker and Nigam, 1998), we next asked if IP₃R-mediated calcium release is required for local TJ remodeling. To test this, we used a highly-specific IP₃R blocker, Xestospingin C (XeC). First, we evaluated the efficiency of XeC in blocking IP₃R-mediated calcium release using an epithelial wound healing assay. Laser wounding of the epithelial cell cortex resulted in the rapid progression of a calcium wave. XeC significantly decreased the amplitude and progression of the calcium wave compared with vehicle (DMSO) controls (Fig. S3, C–C''), as previously reported (Soto et al., 2013). We next tested the effect of XeC on calcium dynamics during local TJ remodeling by performing junctional laser injury (see Fig. 2). Blocking IP₃R-mediated calcium release had no significant effect on the calcium flash or F-actin accumulation at the site of laser-induced TJ leaks (Fig. S3, D and E). Thus, IP₃R-mediated calcium release is not required for local TJ remodeling.

Mechanical stimuli induce Rho flares

We previously reported that naturally-occurring Rho flares are correlated with elongation of cell-cell junctions prior to the flare (Stephenson et al., 2019); however, it remains untested whether junction elongation is a mechanical stimulus that can induce calcium flashes and Rho flares. First, we measured changes in junction length and intracellular calcium at junctions with naturally occurring Rho flares and found that junction elongation initiates ~200 s before the start of the calcium flash, and a rapid

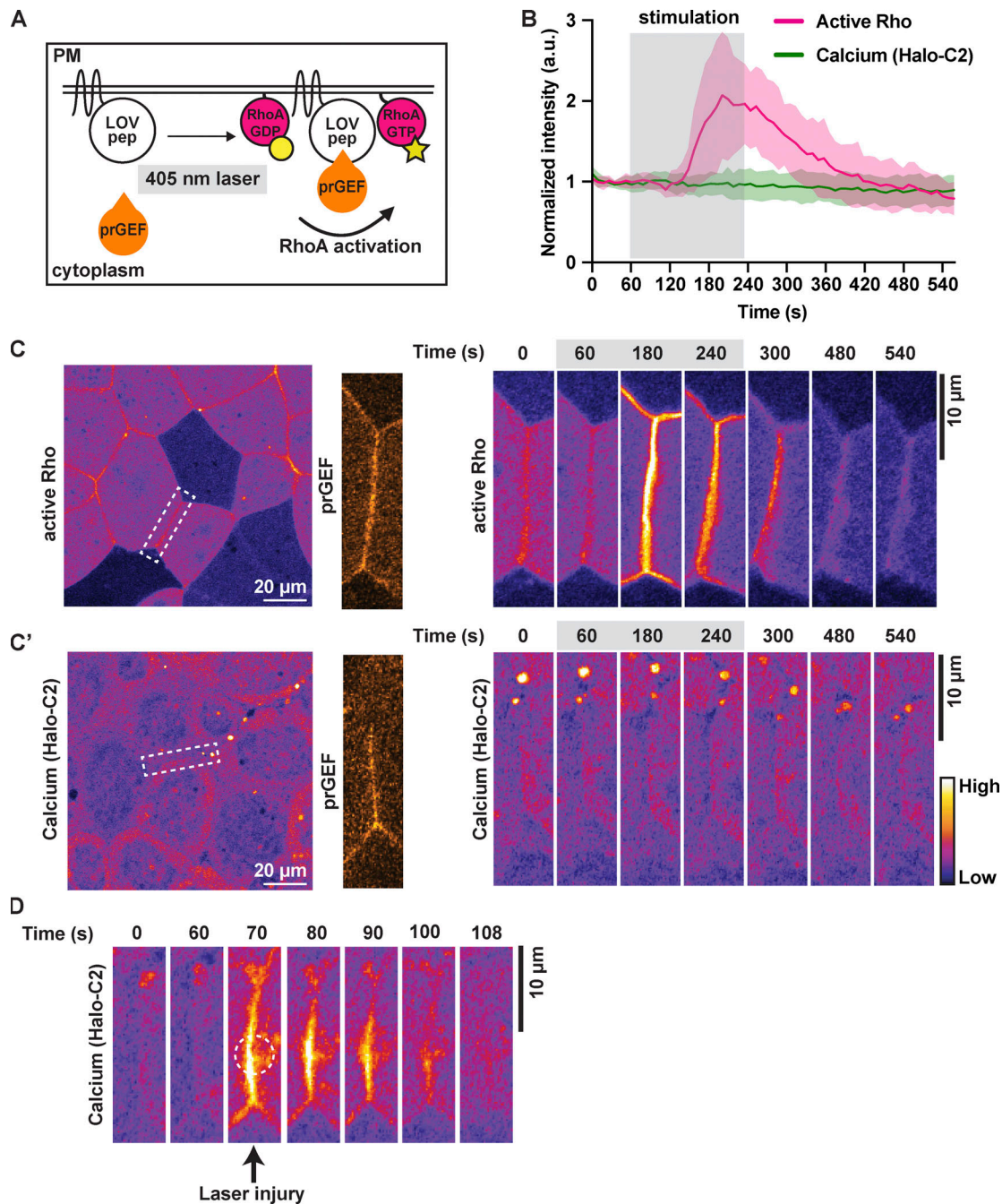


Figure 3. Optogenetic activation of junctional RhoA is not sufficient for local calcium increase. (A) Schematic of TULIP-mediated optogenetic activation of RhoA by the recruitment of a prGEF upon 405-nm laser stimulation. **(B)** Quantification of experiments in C. Mean normalized intensity of active Rho (mCherry-2xrGBD) and calcium (Halo-PKC β -C2, Janelia Fluor 549 HaloTag) upon junction-specific 405-nm laser stimulation (gray box, 60–240 s). Shaded region represents SEM. Active Rho: $n = 10$ junctions, 5 embryos, 3 experiments; calcium (Halo-C2): $n = 12$ junctions, 7 embryos, 3 experiments. **(C)** Left: Cell view of an embryo expressing active Rho probe (mCherry-2xrGBD, FIRE LUT) with ROI for light stimulation indicated by white dashed box. Zoomed image of prGEF (orange LUT) localization at ROI. Right: Time-lapse montage of active Rho probe within the ROI that is stimulated with a 405-nm laser (gray box indicates duration of stimulation). **(C')** Left: Cell view of an embryo expressing active calcium probe (Halo-PKC β -C2, Janelia Fluor 549 HaloTag, FIRE LUT) with ROI for light stimulation indicated by white dashed box. Zoomed image of prGEF (orange LUT) localization at ROI. Right: Time-lapse montage of calcium probe (Halo-C2) within the ROI that is stimulated with a 405-nm laser (gray box indicates duration of stimulation). **(D)** Time-lapse montage of the junction highlighted in C' expressing calcium probe (Halo-PKC β -C2, Janelia Fluor 549 HaloTag, FIRE LUT). Laser injury of the junction resulted in a local calcium increase at the site of the injury. Dashed white circle represents the site of junction injury at time 70 s.

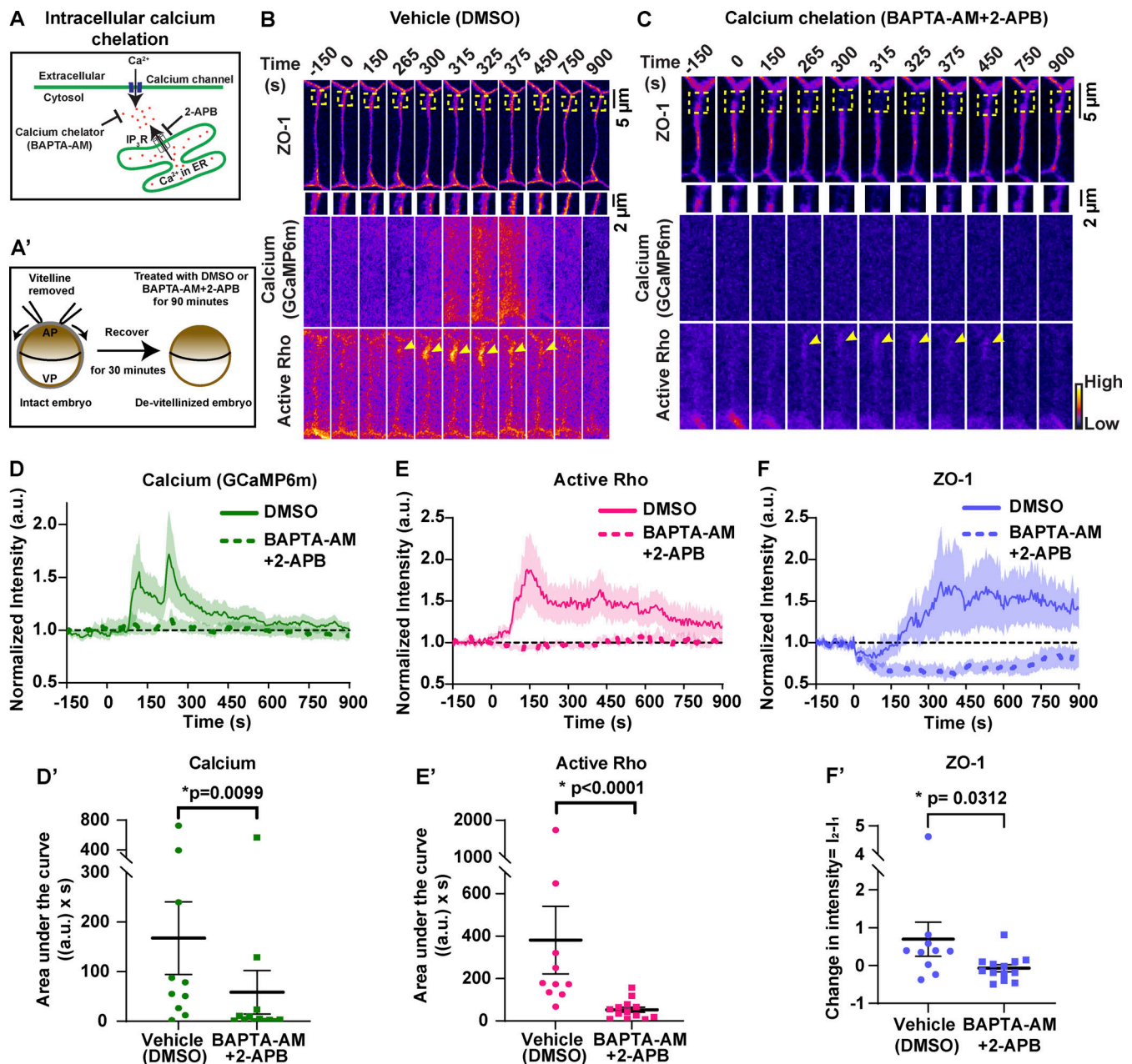


Figure 4. Intracellular calcium flash is required for Rho flare activation and ZO-1 reinforcement. (A) Schematic of cytosolic calcium chelation using BAPTA-AM and blocking IP₃R-mediated calcium release from the ER using 2-APB. (A') Schematic showing BAPTA-AM and 2-APB treatment after removal of vitelline envelope. (B and C) Time-lapse images (FIRE LUT) of BFP-ZO-1, calcium (GCaMP6m), and active Rho (mCherry-2xrGBD). Embryos were treated with 0.5% DMSO (vehicle; B) or 20 μ M BAPTA-AM and 100 μ M 2-APB (calcium chelation; C). Calcium chelation resulted in more severe ZO-1 breaks (yellow boxes, enlarged below) and decreased Rho activity (yellow arrowheads) at the site of ZO-1 loss. Time 0 s represents the start of ZO-1 decrease. (D-F) Graphs of mean normalized intensity of calcium (GCaMP6m; D), active Rho (E), and ZO-1 (F) at the site of ZO-1 loss over time in vehicle (DMSO, solid lines) or calcium chelation (BAPTA-AM + 2-APB, dashed lines) embryos. Shaded region represents SEM. DMSO: $n = 10$ flares, 7 embryos, 7 experiments; BAPTA-AM + 2-APB: $n = 13$ flares, 8 embryos, 8 experiments. (D'-F') Area under the curve (AUC) for calcium (D') and active Rho (E') was calculated from D and E, respectively. Scatter plot of change in ZO-1 intensity (F') was calculated from F. I_1 and I_2 represent average intensity of ZO-1 from individual traces from times 0–50 s and 400–450 s, respectively. Error bars represent mean \pm SEM; significance calculated using Mann-Whitney U test.

contraction of the junction immediately follows the calcium flash (Fig. 5 A). To test if artificially activated junction elongation can induce Rho flares, we optogenetically induced regional contraction to promote junction elongation in the neighboring region. Embryos were injected to achieve mosaic expression of the optogenetic constructs (Fig. 5, B and C). Cells expressing

prGFP were regionally stimulated with 405-nm blue light (Fig. 5 B, gray dotted box), and the frequency of Rho flares was observed in the unstimulated neighboring region (Fig. 5 B, region of observation). The frequency of Rho flares in the region of observation significantly increased post-stimulation compared with prestimulation (Fig. 5, C' and D). Furthermore, optogenetically

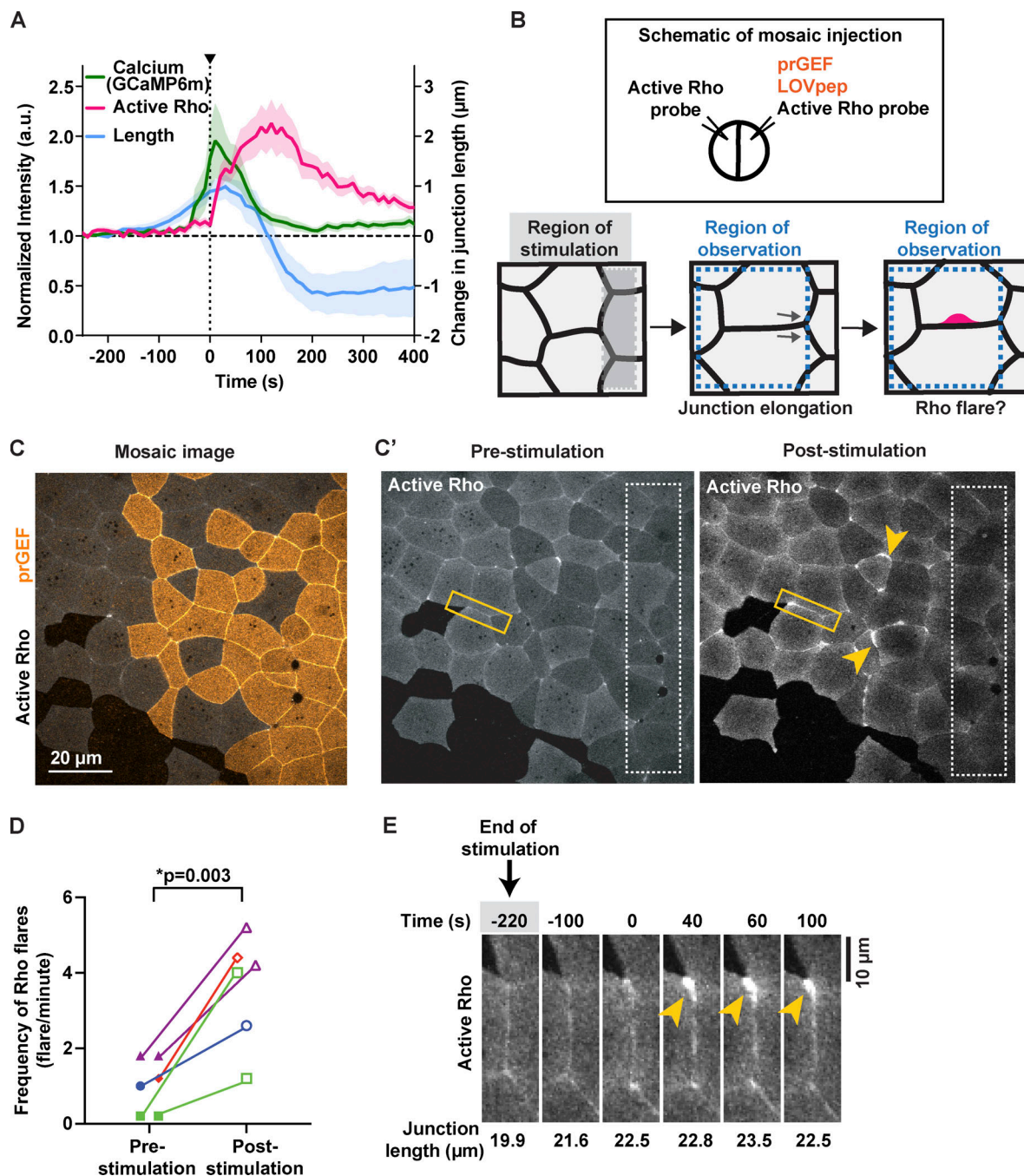


Figure 5. Junction elongation induces Rho flares. (A) Graph showing that calcium flash (GCaMP6m) follows junction elongation (vertex-to-vertex length) and precedes Rho-mediated junction contraction and stabilization of length. Time 0 s represents start of Rho flare. Shaded region represents SEM; $n = 16$ flares, 13 embryos, 10 experiments. (B) Schematic of mosaic injection and regional activation of Rho-mediated contractility using optogenetics. Top: Schematic showing the mosaic injection of optogenetic constructs (prGEF and LOVpep) injected into one cell, while active Rho probe is injected in both cells at two-cell stage. Bottom: Regional activation of RhoA using optogenetics in region of stimulation (shaded gray box) and quantification of junction length and frequency of Rho flares in region of observation (dotted blue box). (C) Cell view of an embryo mosaically-expressing prGEF (2xPDZ-YFP-LARG(DH), yellow) and active Rho probe (mCherry-2xrGBD, gray). (C') Cell view of Rho probe in the embryo from C. Regional stimulation (white dashed box) induces Rho flares in areas neighboring the region of stimulation (yellow arrowheads). (D) Quantification of Rho flares in the area outside the region of stimulation shown in C'. Frequency of Rho flares occurring pre-stimulation (0–300 s) and post-stimulation (600–900 s) are matched for color and shape. Significance calculated using unpaired two-tailed t test; $n = 6$ embryos, 4 experiments. (E) Time-lapse montage of a junction highlighted in C' (yellow box) expressing active Rho probe (mCherry-2xrGBD). Following optogenetic stimulation (indicated by gray shaded box), an increase in junction length precedes Rho flare activation (yellow arrowhead). Junction length measured from vertex to vertex is indicated under each panel.

induced Rho flares were also preceded by junction elongation (Fig. 5 E). Taken together, our data suggest that junction elongation is a mechanical stimulus that induces Rho flares.

MSC-dependent calcium influx is required for Rho-mediated reinforcement of ZO-1

Rho flares are preceded by junction elongation (Fig. 5) and by loss of ZO-1 (Fig. 2 D), a scaffolding protein that connects TJ transmembrane proteins to the underlying actin cytoskeleton. Additionally, Rho flares are accompanied by apical PM deformation (Stephenson et al., 2019), suggestive of the membrane-cortex detachment that precedes blebs in isolated cells. These data, along with the observation that calcium increases originate from the junctional PM (Fig. 1 C and S1 D), suggest that calcium influx may be mediated by MSCs at the junctional PM.

To test this idea, we first evaluated the temporal association of membrane protrusion (tagBFP-membrane) and Rho flares (mCherry-2xrGBD). A kymograph at the site of a Rho flare illustrates that membrane protrusion (blue, Fig. 6 A) expands with a similar timing to the increase in Rho activation (Fig. 6 A, magenta), supporting a mechanosensation-based mechanism. To test if MSCs are responsible for the calcium flash preceding Rho flares, we blocked MSCs using grammostola mechanotoxin #4 (GsMTx4), a peptide from spider venom. GsMTx4 decreases the sensitivity of MSCs to changes in membrane tension, thereby blocking calcium influx mediated by Piezo1 and TRP channels (Fig. 6 B; Bae et al., 2011; Bowman et al., 2007; Gnanasambandam et al., 2017). MSC-mediated calcium transients are required for tissue homeostasis and proper development (Hunter et al., 2014). Therefore, we used GsMTx4 at a low concentration such that embryos successfully develop to gastrula stage and the overall morphology of cell–cell junctions is not altered. GsMTx4 treatment did not alter active RhoA accumulation at the contractile ring in dividing cells (Fig. S4 A), baseline junctional active RhoA (Fig. S4, B and B'), downstream targets of active RhoA (Fig. S4, C–C''), or AJs (Fig. S4, D and D'). However, GsMTx4 treatment significantly decreased the calcium flash associated with Rho flares (Fig. 6, C–E'), indicating that the calcium flashes preceding Rho flares are mediated by MSCs. Further, GsMTx4 treatment decreased the amplitude and duration of Rho flares compared with vehicle (water) controls (Fig. 6, C, D, F, and F'). Although both vehicle- and GsMTx4-treated embryos showed an initial increase in active Rho at the site of ZO-1 loss, Rho flares were lower in intensity and shorter-lived in GsMTx4-treated embryos (Fig. 6 F). In addition, the amount of ZO-1 loss before Rho activation was comparable between vehicle- and GsMTx4-treated embryos (Fig. 6 G, I₁). However, treatment with GsMTx4 significantly reduced ZO-1 reinforcement compared with vehicle controls (Fig. 6, C, D, G, and G'). Together, these findings demonstrate that MSC-mediated calcium influx is required for robust Rho flare activation and efficient reinforcement of ZO-1.

MSC-mediated calcium influx is critical for epithelial barrier function and local junction contraction

Rho flare-mediated ZO-1 reinforcement is required to repair local leaks and maintain paracellular barrier integrity. Our results show that a calcium increase follows local leaks (Figs. 1 B

and 2 E), and blocking MSCs leads to impaired Rho activation and ZO-1 reinforcement (Fig. 6, F and G). Therefore, we hypothesized that MSC-mediated calcium influx is required to maintain an intact paracellular epithelial barrier. To detect transient leaks in the barrier, we performed ZnUMBA in vehicle- or GsMTx4-treated embryos. With GsMTx4 treatment, the whole-field intensity of FluoZin-3 increased over time compared with vehicle controls (Fig. 7, A and B), indicating a global barrier disruption. This barrier disruption could be the result of failure to repair local leaks associated with ZO-1 loss. As local barrier leaks were followed by Rho flares in control embryos, we used Rho flares as an indicator of sites of local leaks (Stephenson et al., 2019) and analyzed the frequency of Rho flares in vehicle- and GsMTx4-treated embryos. Notably, we found that the frequency of Rho flares increased significantly in GsMTx4-treated embryos compared with matched controls (Fig. 7 C and Video 9), suggesting an increase in local leaks. To examine if local leaks were contributing to global barrier disruption, we analyzed individual junctions exhibiting local FluoZin-3 increases. With GsMTx4 treatment, local FluoZin-3 increased repeatedly at the site of ZO-1 loss (Fig. 7 E, single and double white arrows) compared with vehicle controls, in which the local FluoZin-3 increase was resolved after robust activation of Rho flares and ZO-1 reinforcement (Fig. 7, D and E; and Video 10). Of note, in GsMTx4-treated embryos, Rho flares often failed to be activated following an increase in local FluoZin-3 (Fig. 7 E, yellow arrow). Collectively, these findings suggest that MSC-mediated robust activation of Rho flares and ZO-1 reinforcement are required to resolve local leaks to maintain the overall paracellular barrier integrity.

After TJ breaks, Myosin II activation through a Rho/ROCK-mediated signaling pathway is required for efficient ZO-1 reinforcement via local junction contraction (Stephenson et al., 2019). We next asked whether reduced ZO-1 reinforcement observed in GsMTx4-treated embryos was a result of reduced junction contraction. We found that the characteristic rapid contraction of the junction immediately following the Rho flare was significantly reduced in GsMTx4-treated embryos compared with vehicle controls (Fig. 7, F and F'). To track the local contractile regions within individual junctions, we generated kymographs of cell–cell junctions projected from vertex to vertex. In GsMTx4-treated embryos, we observed a dramatic loss of junction contraction and lack of ZO-1 reinforcement following Rho flares (black bracket, Fig. 7 G) compared with robust contraction and ZO-1 reinforcement in controls. Additionally, kymographs highlighted that in GsMTx4-treated embryos, there are many short-lived Rho flares, which often repeat at the same site and yet remain unable to reinforce ZO-1 (orange arrows, Figs. 7 G and S5 A). Furthermore, we observed reduced F-actin accumulation at the sites of short-lived Rho flares in GsMTx4-treated embryos (Fig. S5, B and C). Taken together, our results show that MSC-mediated calcium influx is required for local junction contraction and efficient TJ reinforcement following barrier leaks through robust and sustained Rho activation.

Discussion

Epithelial tissues adapt to mechanical stimuli by remodeling their cell–cell junctions and associated cytoskeleton to maintain

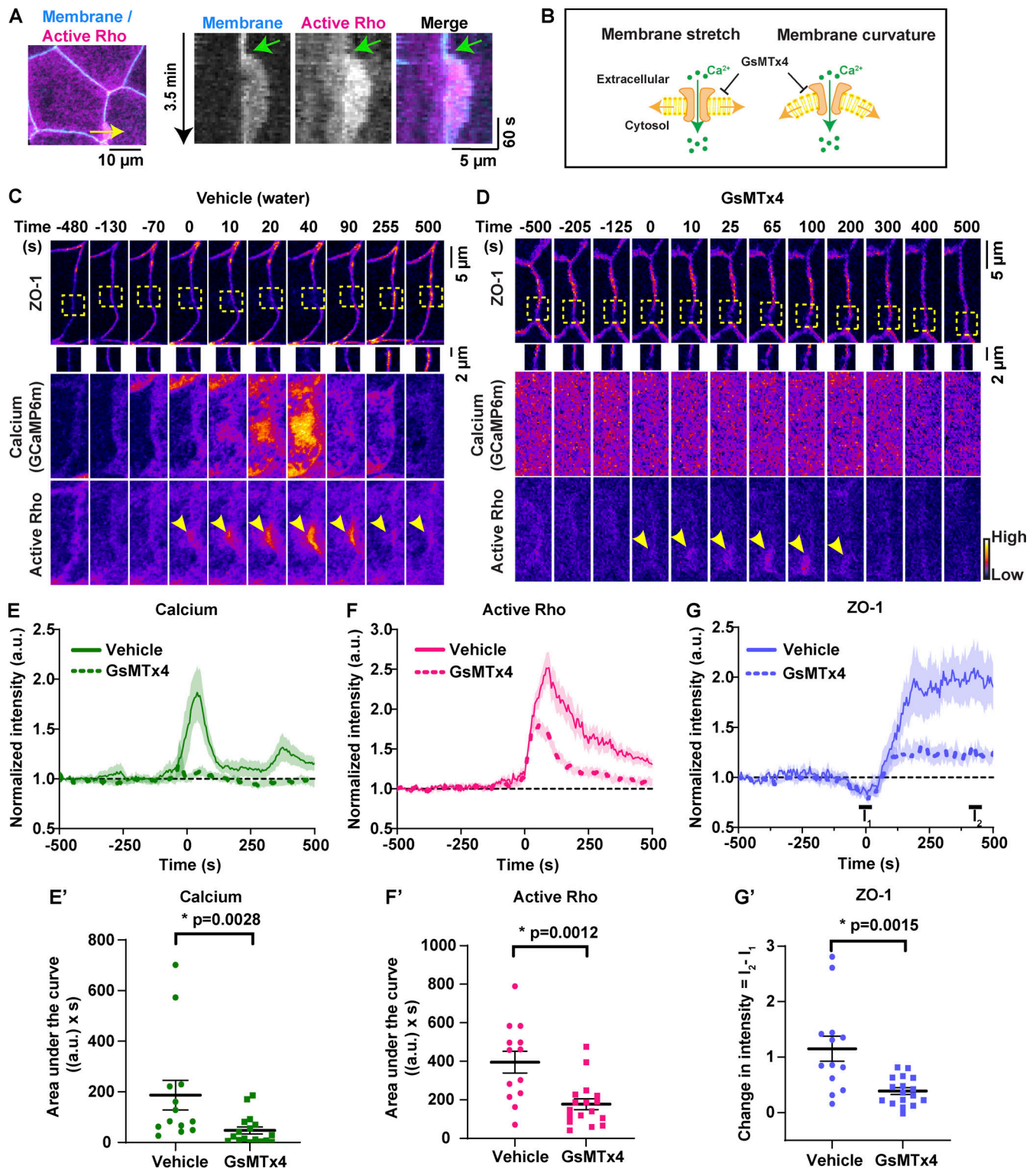


Figure 6. **MSC-dependent calcium influx is required for Rho-mediated reinforcement of ZO-1.** (A) Left: Cell view of an embryo expressing membrane probe (membrane-tagBFP, cyan) and active Rho probe (mCherry-2xrGBD, magenta). Yellow arrow indicates the 2-pixel-wide region used to generate the kymograph. Right: Kymograph shows that membrane protrusion increases with Rho flare. Green arrow indicates the start of membrane protrusion and Rho flare. (B) Schematic showing that GsMTx4 inhibits MSC-mediated calcium influx in response to changes in membrane tension induced by membrane stretch or curvature. (C and D) Time-lapse images (FIRE LUT) of BFP-ZO-1, calcium (GCaMP6m), and active Rho (mCherry-2xrGBD). Embryos were treated with water (vehicle; C) or 12.5 μ M GsMTx4 (MSC inhibitor; D). MSC inhibition resulted in a decrease in calcium influx; short-duration, low-intensity Rho flares (yellow arrowheads; D); and decreased ZO-1 reinforcement at the site of ZO-1 loss (yellow boxes, enlarged below; D). Time 0 s represents the start of Rho flares. (E–G) Graphs of mean normalized intensity of calcium (GCaMP6m; E), active Rho (F), and ZO-1 (G) at the site of ZO-1 loss over time in vehicle- (water, solid lines) or MSC-inhibited (GsMTx4, dashed lines) embryos. Shaded region represents SEM. Vehicle: $n = 13$ flares, 6 embryos, 6 experiments; GsMTx4: $n = 17$

flares, 7 embryos, 6 experiments. (**E'–G'**) AUCs for calcium (E') and active Rho (F') were calculated from E and F , respectively. (**G'**) Scatter plot of change in ZO-1 intensity (G') was calculated from G . I_1 and I_2 represent average intensity of ZO-1 from individual traces at times -25 to 25 s and 400 – 450 s, respectively. Error bars represent mean \pm SEM; significance calculated using Mann–Whitney U test.

tissue homeostasis and barrier function. We previously showed that physiological mechanical stimuli, such as the junction elongation that happens in response to cell shape changes, cause short-lived, local paracellular leaks (Stephenson et al., 2019). However, it was unclear how cells sense local leaks. In this study, we identified that mechanosensitive calcium signaling is a key player initiating Rho flare-mediated repair of TJs (Fig. 7 H).

Calcium flashes are a consequence of local barrier leaks and promote barrier repair

In epithelial cells, a range of spatiotemporal calcium transients have been observed including waves, flashes, flickers, and puffs (Balaji et al., 2017; Brodskiy and Zartman, 2018). Using genetically encoded calcium probes, we identified intracellular calcium flashes during TJ remodeling. Calcium flashes originated at the junctional PM after a local loss of TJ proteins and a barrier breach during both naturally occurring and experimentally induced barrier leaks. Previous studies have shown that intracellular calcium signaling is critical for formation of TJs and establishment of barrier function during TJ biogenesis (Gonzalez-Mariscal et al., 1990; Nigam et al., 1992). However, the timescale of TJ formation following a calcium increase in these studies is significantly slower (~ 50 min) compared with the rapid reinstatement of TJs following the calcium flashes described here (~ 1 – 2 min). In contrast to the TJ biogenesis work and our findings, whole-cell intracellular calcium increases in mature epithelia can lead to barrier dysfunction (Elamin et al., 2014). Our study reveals that local intracellular calcium flashes are a consequence of paracellular leaks and contribute to TJ repair rather than barrier dysfunction.

Intracellular calcium transients exhibit a wide range of spatiotemporal dynamics based on the source of calcium increase and scale of remodeling events (Balaji et al., 2017; Clark et al., 2009; Soto et al., 2013). The long- and short-range calcium waves observed in epithelial cells are primarily mediated by IP_3 -dependent release of calcium from the ER (Balaji et al., 2017; Jaffe, 2008; Soto et al., 2013; Wallingford et al., 2001; Webb and Miller, 2006). In contrast, localized calcium transients are generally mediated by PM-localized calcium channels, thereby creating a local calcium increase near the opening of the channel, called a “calcium microdomain” (Berridge, 2006; Tsai et al., 2015; Wei et al., 2009). In our study, local calcium flashes associated with TJ remodeling originate close to the junctional PM, consistent with forming a calcium microdomain near the PM, suggesting a role for PM-localized calcium channels. An alternate explanation for these local calcium flashes would be a local membrane rupture; however, previous work from our lab suggests that the PM is indeed intact at the site of leak (Stephenson et al., 2019). Additionally, multiple pieces of evidence suggest that calcium flashes are independent of IP_3 -mediated calcium release from the ER. First, the duration of calcium flashes during TJ remodeling is longer (~ 65 – 85 s) than calcium flashes

mediated by intracellular calcium stores during apical constriction in *Xenopus* (~ 26 – 40 s; Christodoulou and Skourides, 2015; Suzuki et al., 2017). Second, blocking IP_3 R-mediated calcium release from the ER had no effect on the dynamics of calcium flashes or the repair of the barrier leaks. Finally, we noted that when cells exhibited calcium transients generally associated with calcium release from the ER (higher amplitude that is not sustained or a uniform increase throughout the cell), TJ leaks failed to be repaired. It remains possible, however, that calcium flashes could induce calcium release from ER independently of IP_3 R. In contrast to our findings, it has been reported that in mature epithelia, intracellular calcium increase mediated by IP_3 R can lead to barrier dysfunction (Elamin et al., 2014), indicating that intracellular calcium can have opposing effects on barrier function based on the spatial and temporal dynamics of the calcium signal, thus highlighting the importance of identifying the role of calcium signaling in diverse physiological contexts.

Crosstalk between calcium and RhoA

Both calcium transients and RhoA activation are modulated locally and globally in response to mechanical stimuli (Acharya et al., 2018; Benink and Bement, 2005; Clark et al., 2009; Pardo-Pastor et al., 2018). Our results demonstrate that the intensity of intracellular calcium flashes and Rho flares are positively correlated, and calcium reaches peak intensity before Rho. Further, we observed that perturbation of intracellular calcium using either a cytoplasmic calcium chelator in conjunction with an IP_3 R blocker (BAPTA-AM + 2-APB), or a MSC blocker (GsMTx4) significantly reduced the intensity and duration of RhoA flares at sites of ZO-1 loss. Interestingly, treatment with BAPTA-AM + 2-APB showed a stronger effect compared with GsMTx4. The differences could potentially be due to altered tissue tension resulting from physical removal of the vitelline for BAPTA-AM + 2-APB but not GsMTx4 experiments, a calcium-independent effect of BAPTA-AM on the actin cytoskeleton (Saoudi et al., 2004), or off-target inhibition of TRP channel-mediated calcium influx by 2-APB (Takeuchi et al., 2020; Zhang et al., 2017). We also demonstrate that optogenetic local activation of RhoA at TJs is not sufficient to induce a local calcium increase, supporting the notion that calcium is acting upstream of Rho in this case. Together, our evidence demonstrates that intracellular calcium flashes positively regulate the activity of RhoA during TJ remodeling.

The mechanism by which calcium regulates RhoA activity remains unknown. Our results show that despite the spreading of calcium throughout the cell, Rho flares are spatially confined to the site of paracellular leaks. This suggests that calcium may regulate RhoA activity by modulating the activity of a specific Rho GEF or Rho GAP, rather than direct regulation of RhoA. Potential mechanisms by which intracellular calcium increase could activate RhoA include $PKC\alpha$ -mediated activation of a Rho

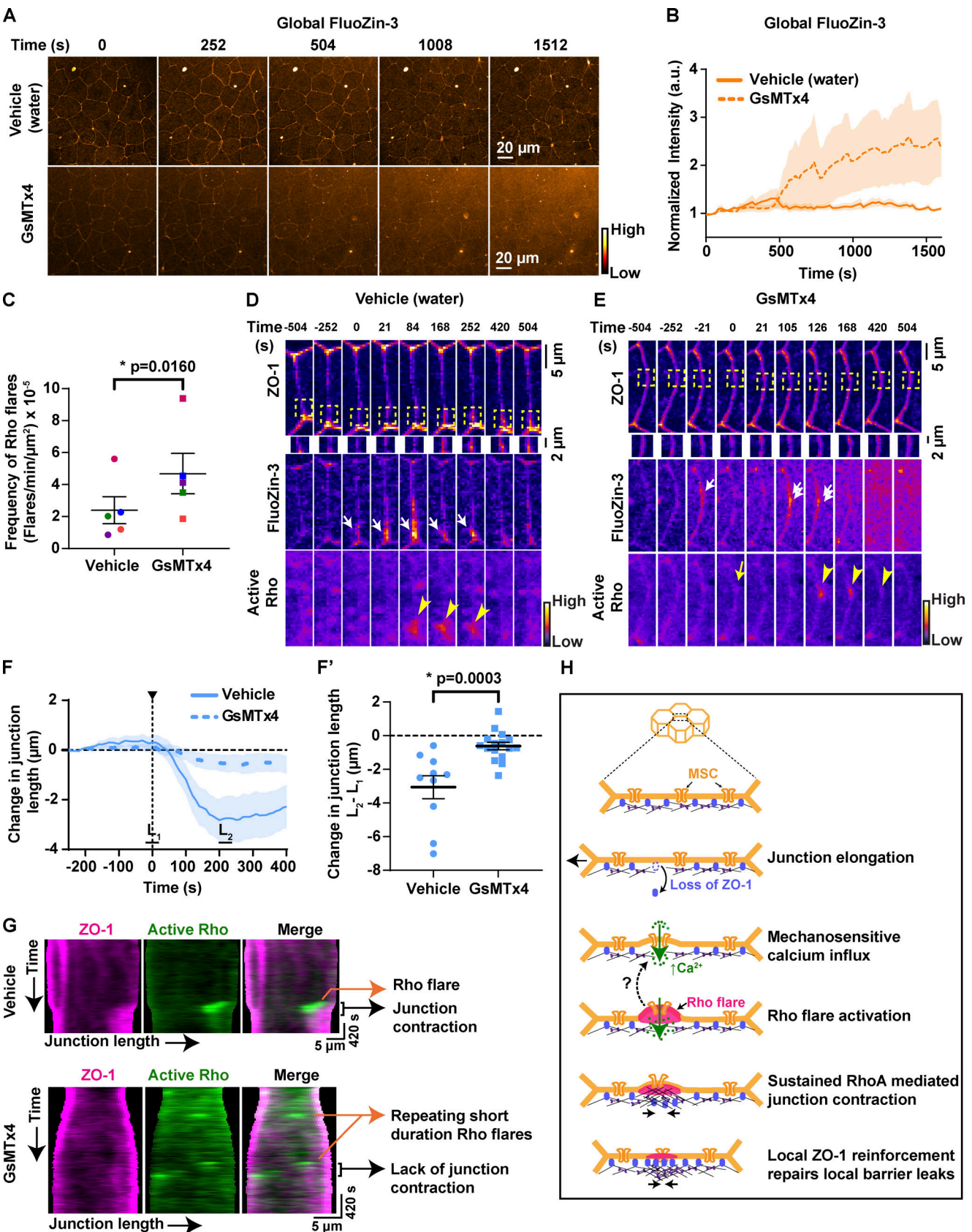


Figure 7. **MSC-mediated calcium influx is critical for epithelial barrier function and local junction contraction.** (A) Time-lapse images (orange hot LUT) of epithelial permeability tested using ZnUMBA (FluoZin-3). Embryos were treated with water (vehicle, top) or 12.5 μM GsMTx4 (MSC inhibitor, bottom). Time 0 s represents the start of the time-lapse movie. (B) Graph of mean normalized intensity of whole-field FluoZin-3 for vehicle (water) or GsMTx4-treated

embryos. Blocking MSCs increased global FluoZin-3 intensity over time compared with vehicle. Shaded region represents SEM. Vehicle: $n = 6$ embryos, 4 experiments; GsMTx4: $n = 6$ embryos, 4 experiments. **(C)** Frequency of Rho flares in vehicle- (water) and GsMTx4-treated embryos. Frequencies from paired experiments are color matched. Error bars represent mean \pm SEM; significance calculated using paired two-tailed t test; $n = 5$ embryos, 4 experiments. **(D and E)** Montage of representative junctions from A (FIRE LUT). Blocking MSCs with GsMTx4 causes repeated increases in local FluoZin-3 (white arrows), reduced ZO-1 (BFP-ZO-1) reinforcement (yellow boxes, enlarged below), and reduced duration of Rho flares (mCherry-2xrGBD, yellow arrowheads) at sites of ZO-1 loss. Repeated FluoZin-3 increase is indicated by double white arrows, and failure to activate Rho flare after FluoZin-3 increase is indicated by yellow arrow. **(F and F')** Graph of change in junction length for junctions with Rho flares in vehicle- (water) and GsMTx4-treated embryos. Shaded region represents SEM. **(F')** Scatter plot of change in junction length was calculated from F. L_1 and L_2 represent average length of junction from individual traces from times -20 to 20 s and 200 – 240 s, respectively. Error bars represent mean \pm SEM; significance calculated using Mann–Whitney U test. Vehicle: $n = 10$ flares, 6 embryos, 6 experiments; GsMTx4: $n = 16$ flares, 7 embryos, 6 experiments. **(G)** Kymographs of BFP-ZO-1 (magenta) and active Rho (mCherry-2xrGBD, green) from representative junctions projected vertex to vertex over time for vehicle- (water) and GsMTx4-treated embryos. Kymographs highlight the repeating, short-duration Rho flares, loss of local junction contraction, and reduced ZO-1 reinforcement upon GsMTx4 treatment. **(H)** Model showing mechanism by which mechanosensitive calcium signaling regulates epithelial barrier function. Top: 3D view of epithelial cells. Bottom: En face view of the junction highlighted showing our model of the local calcium and RhoA signaling following mechanical stimuli. Dotted arrow indicates a possible positive feedback mechanism where active RhoA-mediated membrane protrusion regulates MSC-dependent calcium influx at the site of ZO-1 repair, thus helping to sustain local Rho activation.

GEF (Holinstat et al., 2003) or CaMKII-mediated crosstalk between active Cdc42 and RhoA (Benink and Bement, 2005; Murakoshi et al., 2011). Alternatively, an intracellular calcium increase could sustain RhoA activation by increasing the residence time of RhoA at the PM in an Anillin-dependent manner (Budnar et al., 2019). In agreement with this idea, we previously showed that knockdown of Anillin leads to short-lived Rho flares (Reyes et al., 2014), similar to GsMTx4-treated cells observed in this study. These findings suggest that calcium might increase the residence time of junctional active RhoA in an anillin-dependent manner by enriching PIP_2 at the PM (Wang and Richards, 2012) or binding C2 domain of Anillin (Cho and Stahelin, 2006; Sun et al., 2015). Finally, it is possible that the initial activation of Rho flares is independent of calcium influx; however, the sustained activation of Rho flares is dependent on MSC-mediated local calcium increase (Fig. S5 D).

In addition to regulating RhoA activity, MSC-mediated local calcium increase is important for reinforcement of ZO-1, as both intracellular calcium chelation and blocking MSCs inhibited reinforcement of ZO-1. We show that this lack of ZO-1 reinforcement is due to reduced RhoA-mediated junction contraction, presumably due to reduced ROCK/Myosin II activation at the site of leaks (Stephenson et al., 2019). Additionally, biochemical studies have demonstrated that intracellular calcium increase (Stuart et al., 1994) and active RhoA (Nusrat et al., 1995) are required for the association of ZO-1 with the actin cytoskeleton. Notably, our work is the first to demonstrate that intracellular calcium promotes recruitment and reinforcement of ZO-1 at TJs via regulating RhoA activation. Further, given that myosin light chain kinase (MLCK) is activated by calcium/calmodulin (Heissler and Sellers, 2014), and active MLCK stabilizes ZO-1 at TJs (Yu et al., 2010), it is also possible that calcium regulates ZO-1 reinforcement at TJs via MLCK activation in parallel to RhoA activation.

Mechanical stimuli activate MSCs at local sites

Using a broad MSC-blocker (GsMTx4), we demonstrated that calcium flashes are mediated by MSCs during TJ remodeling. In addition to being activated by externally applied mechanical stimuli, MSCs can be activated from inside the cell by cytoskeleton-generated tension and/or changes in cortical tension (Heisenberg, 2017; Nourse and Pathak, 2017; Shi et al., 2018;

Welf et al., 2020). Given that calcium flashes follow junction elongation, and junction elongation is a mechanical stimulus that induces Rho flares (Fig. 5), it seems likely that MSCs are activated by changes in membrane tension as junctions elongate (Liu and Montell, 2015; Orr et al., 2006; Shi et al., 2018). However, the location and timing of calcium flashes supports the idea that MSCs are not activated along the entire length of the elongating junction, but instead at local sites.

It remains unknown which MSC is responsible for the calcium flashes associated with TJ remodeling. Several MSCs belonging to the Piezo and TRP families, including Piezo1, TRPC1, TRPC5, TRPC6, TRPV2, and TRPV4, are known to be expressed in epithelial tissues (Akazawa et al., 2013; Coste et al., 2010; Miyamoto et al., 2014; Tiruppathi et al., 2006; Weber and Muller, 2017). GsMTx4 blocks calcium influx mediated by Piezo1 and members of the TRP family, specifically TRPC6 and TRPV4 (Bae et al., 2011; Bowman et al., 2007; Spassova et al., 2006), and 2-APB can block TRPC6 and TRPV4 (Takeuchi et al., 2020; Zhang et al., 2017). Thus, it will be of high interest to define the roles of Piezo1 and TRP channels in TJ remodeling.

Rho flares follow TJ leaks and are associated with apical membrane protrusions (Fig. 6), displaying a change in membrane curvature (Stephenson et al., 2019) and likely a change in membrane tension. However, it is not clear if the membrane protrusions observed during Rho flares are bleb-like or lamellipodia-like protrusions. Bleb-like protrusions occur where the connection of the PM to the underlying actin cortex is weakened or lost (Charras, 2008), whereas lamellipodia-like protrusions occur when Arp2/3-mediated branched actin pushes the membrane outward (Taha et al., 2014). While the growth phase of typical blebs is devoid of cytoskeletal elements in the protrusion and is pushed out due to intracellular pressure, the membrane protrusion observed during Rho flares has a homogeneous distribution of active Rho and F-actin (Figs. 6 and S5 B). We speculate that Rho flares might follow a combination model, in which the initiation phase follows a bleb-like pattern due to local uncoupling of the membrane from the underlying actin cortex upon loss of ZO-1, followed by a formin- and Arp2/3-mediated actin-based protrusion model during the growth phase. In agreement with our idea, a recent study showed that initial detachment of the actin cortex from the membrane is required for initiation of both bleb-like and F-actin-mediated protrusions

(Welf et al., 2020). Given that membrane protrusions are reported to be sites of increased membrane tension (Shi et al., 2018), and that the growth phase of membrane protrusions is dependent on cytoskeletal-mediated cortical tension (Tinevez et al., 2009), future studies should investigate the roles that local membrane tension and cortical actin attachment and uncoupling play in the initiation and repair of barrier leaks.

MSC-mediated regulation of the TJ barrier

Expression and activity of MSCs, including Piezo1 and TRPV4, have been shown to enhance global barrier function (Akazawa et al., 2013; Sokabe et al., 2010; Zhong et al., 2020). Consistent with this finding, using live imaging and a highly sensitive barrier assay, we showed that MSC-mediated calcium influx is required to maintain global barrier function. Interestingly, the increased global paracellular permeability observed with the MSC blocker GsMTx4 appears to be a cumulative effect of failure to fix local leaks. When MSCs were blocked, Rho flares often failed to be activated immediately following the leak, and when Rho flares were weakly activated, they tended to repeat at the site of the leaks in failed attempts to reinforce ZO-1.

In conclusion, this study demonstrates that mechanically-triggered calcium influx is an important feature of the mechanism by which epithelial cells sense and respond to transient leaks in barrier function (Fig. 7 H). Calcium flashes mediated by MSCs are required for local junction contraction through robust and sustained Rho activation, and this is necessary for efficient TJ reinforcement. When MSCs are blocked, local leaks fail to be repaired by low intensity, short duration Rho flares, and global barrier function is disrupted. Thus, MSC-mediated local calcium influx may serve as a mechanotransduction mechanism to relay biochemical signals specifically to sites of local paracellular leaks without affecting overall TJ structure and function, thereby allowing epithelial cells to undergo dynamic cell shape changes yet maintain barrier function.

Materials and methods

DNA constructs

GCaMP6m was generated by PCR amplifying the GCaMP6m sequence from pGP-CMV-GCaMP6m (Addgene plasmid #40754; Chen et al., 2013) and ligating it into the BamHI and EcoRI sites in pCS2+. BFP-PKC- β -C2 and mNeon-PKC- β -C2 were generated by PCR amplifying the C2 domain of *Xenopus* PKC- β from pCS2+/eGFP-PKC- β -C2 (Yu and Bement, 2007) and ligating into the XhoI and EcoRI sites in pCS2+/N-tagBFP2.0 and pCS2+/N-mNeon. Halo-PKC- β -C2 was generated by PCR amplifying the C2 domain of *Xenopus* PKC- β from mNeon-PKC- β -C2 and ligating into the XbaI and EcoRI sites of pCS2+/N-Halo (see below). Stargazin-GFP-silent-LOVpep (referred to as LOVpep) was a gift from Dr. Patrick Oakes and was cloned into the ClaI site in pCS2+. 2xPDZ-YFP-LARG(DH) (referred to as prGEF) was generated by PCR amplifying the 2XPZDZ-YFP-LARG(DH) sequence from pEGFP-N1-PR_GEF-YFP (Addgene plasmid #80408; Wagner and Glotzer, 2016) and ligating into the ClaI and StuI sites in pCS2+. Stargazin-GFP-LOVpep (referred to as GFP-LOVpep) was generated by PCR amplifying the Stargazin-GFP-

LOVpep sequence (Addgene plasmid #80406; Wagner and Glotzer, 2016) and ligating into the ClaI site in pCS2+. 2xPDZ-mCherry-LARG(DH) (referred to as prGEF-mCherry) was generated by PCR amplifying the 2XPZDZ-mCherry-LARG(DH) sequence from pEGFP-N1-PR_GEF-mCherry (Addgene plasmid #80407; Wagner and Glotzer, 2016) and ligating into the ClaI and XbaI sites of pCS2+. The mCherry sequence was then codon optimized for use in *Xenopus* by modifying the arginine 377 codon (CGG to AGA) using the QuikChange XL Site-Directed Mutagenesis Kit (Agilent #200517). All constructs were verified by sequencing. pCS2+/mCherry-2xrGBD (probe for active Rho; Davenport et al., 2016), pCS2+/BFP-ZO-1 (human ZO-1; Stephenson et al., 2019), pCS2+/R-GECO1 (probe for calcium; Suzuki et al., 2017), pCS2+/Lifeact-GFP (probe for F-actin; Higashi et al., 2016), and pCS2+/BFP-membrane (probe for membrane; Higashi et al., 2016) were previously reported.

Primer sequences used to clone the above constructs into pCS2+ were as follows: pCS2+/GCaMP6m (forward: 5'-AATGGA TCCGCCACCATGGGTTCTCATCATCATCATCATGG-3', reverse: 5'-ATATGAATTCACCTTCGCTGTCATCATTTGTACAAAC TCTTCG-3'); pCS2+/N-tagBFP2.0-PKC- β -C2 (forward: 5'-ATC TCGAGCAATGGGCACTGACCACACCGAGCGCAG-3', reverse: 5'-ATGAATTCACACAGGAACGTTAAAGTATTCTCCCTCCTCCTG-3'); pCS2+/mNeon-PKC- β -C2 (forward: 5'-ATCTCGAGCAAT GGGCACTGACCACACCGAGCGCAG-3', reverse: 5'-ATGAATTCACACAGGAACGTTAAAGTATTCTCCCTCCTCCTG-3'); pCS2+/Halo-PKC- β -C2 (forward: 5'-GCTCCGGACTCAGATCTCGAGCTC AAGCTTcTAATTCATGGGCACTGACCACACC-3', reverse: 5'-TGGATCTACGTAATACGACTCACTAATAGTTCTAGATTACAC AGGAACGTTAAAGTATTCTCC-3'); pCS2+/Stargazin-GFP-LOVpep (forward: 5'-AAAAATCGATACCATGGGGCTGTTTGATCG AG-3', reverse: 5'-TTTTATCGATTTACACCAGGTATCCACCG-3'); pCS2+/2xPDZ-mCherry-LARG(DH) (forward: 5'-CAAGCT ACTTGTCTTTTTGCAGGATCCCATCGATACCGTCGACAATG GCAAAACAAGAGATTG-3', reverse: 5'-GATCTACGTAATACG ACTCACTATAGTTCTAGATTAGCGCTGCTTGTCTTCTGC-3'); pCS2+/2xPDZ-YFP-LARG(DH) (forward: 5'-CAAGCTACTTGT TCTTTTTGCAGGATCCCATCGATACCGTCGACAATGGCAAAA CAAGAGATTG-3', reverse: 5'-CGACTCACTATAGTTCTAGAG GCTCGAGAGGCCTTTAGCGCTGCTTGTCTTCTGC-3'); and pCS2+/Stargazin-GFP-silent-LOVpep (forward: 5'-AAAAATCGATACCAT GGGGCTGTTTGATCGAG-3', reverse: 5'-TTTTATCGATTTACA CCCAGGTATCCACCG-3').

The Halo-tag was codon optimized for use in *Xenopus* using a gBlock from Integrated DNA Technologies and cloned into the BamHI and XhoI sites in pCS2+ using the following primers (forward: 5'-GATTTAGGTGACACTATAGAATACAAGCTACTT GTTCTTTTTGCAGG-3', reverse: 5'-GAGCTCAAGCTTCGAATT CTGCAGTCTAGAACTATAGTGAGTC-3'). gBlock sequence for codon optimized Halo-tag is as follows (codons optimized for *Xenopus* are in lowercase bold): 5'-ATAGAATACAAGCTACTT GTTCTTTTTGCAGGATCCAAACCATGGCAGAAATCGGTACTG GCTTTCCATTGACCCCCATTATGTGGAAGTCTGGGCGAGC GCATGCACTACGTGATGTTGGT**ccca**CGCGATGGCACCCCTGTG CTGTTCTGCACGGTAAC**ccca**ACCTCTCCTACGTGTGGCGAAC ATCAT**ccca**CATGTTGC**ccca**ACCCATCGCTGCATTGTCTCAGAC CTGATCGGTATGGGCAAAATCCGACAAACCAGACCTGGGTTAT

TTCTTCGACGACCACGCTCCGCTTCATGGATGCCTTCATCGAA
 GCCCTGGGTCTGGAAGAGGTCTGCTGGTCATTACGACTGG
 GGCTCCGCTCTGGGTTTCCACTGGGCCAAGCGCAATCCAGAG
 CGCGTCAAAGGTATTGCATTTATGGAGTTCATCCGCCCT
 ATC**cca**ACCTGGGACGAATGGCCAGAATTTGCCCGCAGACC
 TTCCAGGCCTTCCGACCACCGACGTCGGCCGCAAGCTGATC
 ATCGATCAGAACGTTTTTATCGAGGGT**taca**CTG**cca**ATGGGTGT
 CGTCCGC**cca**CTGACTGAAGTCGAGATGGACCATTACCGC
 GAG**cca**TTCCTGAATCCTGTTGACCGCGAGCCACTGTGGCGC
 TTCCCAAACGAGCTGCCAATCGCCGGTGAGCC**agct**AACATCG
 TC**gct**CTGGTCTGAAGAATACATGGACTGGCTGCACCAGTCC
 CCTGT**cca**AAGCTGTCTGTTCTGGGGCACCCAGGCGTTCTG
 ATCCC**acca**GCCGAAGCCGCTCGCCTGGCCAAAAGCCTGCCT
 AACTGCAAGGCTGTGGACATCGGC**cca**GGTCTGAATCTGCTG
 CAAGAAGACAAC**cca**GACCTGATCGGCAGCGAGATC**gct**CGC
 TGGCT**gagcaca**CTCGAGATTTCCGGCTCCGGACTCAGATCT
 CGAGCTCAAGCTTCGAATTCTGCAG-3'.

mRNA preparation

All plasmid DNAs were linearized with NotI, except BFP-ZO-1, which was linearized using KpnI. mRNA was in vitro transcribed from linearized pCS2+ plasmids using the mMessage mMachine SP6 Transcription kit (Ambion) and purified using the RNeasy Mini kit (Qiagen). Transcript size was verified on 1% agarose gel containing 0.05% bleach and Millennium RNA markers (Invitrogen).

Xenopus embryos and microinjection

All studies conducted using *Xenopus* embryos strictly adhered to the compliance standards of the U.S. Department of Health and Human Services Guide for the Care and Use of Laboratory Animals and were approved by the University of Michigan Institutional Animal Care and Use Committee. Eggs from *Xenopus* were collected, in vitro fertilized, and dejellied (Miller and Bement, 2009; Woolner et al., 2009). Dejelled embryos were stored at 15°C in 0.1× Mark's modified Ringer's solution (MMR) containing 10 mM NaCl, 0.2 mM KCl, 0.2 mM CaCl₂, 0.1 mM MgCl₂, and 0.5 mM HEPES, pH 7.4. Embryos were microinjected in the animal hemisphere with mRNA either twice per cell at the two-cell stage or once per cell at the four-cell stage. For optogenetic mosaic injections, embryos were injected with active RhoA probe mRNA once per cell at the four-cell stage, followed by single injections of LOVpep/prGEF mRNAs in two cells at the four-cell stage. Injected embryos were allowed to develop to gastrula stage (Nieuwkoop and Faber stage 10.5–12) at 15°C or 17°C (in the dark for optogenetic mRNA injections). The amount of mRNA per 5 nl of microinjection volume was as follows: BFP-PKC-β-C2, 100 pg; mNeon-PKC-β-C2, 100 pg; GCaMP6m, 500 pg; R-GECO1, 520 pg; Halo-PKC-β-C2, 180 pg with with 20 μM Janelia Fluor 549 HaloTag ligand (#G1110; Promega); LOVpep, 5 pg; prGEF, 2 pg; GFP-LOVpep, 80 pg; prGEF-mCherry, 4 pg; mCherry-2xrGBD, 50 pg; BFP-ZO-1, 50 pg; BFP-membrane, 12.5 pg; and Lifeact-GFP, 10 pg.

Microscope image acquisition

Live imaging of gastrula stage *Xenopus* embryos was performed on an inverted Olympus Fluoview 1000 Laser Scanning Confocal Microscope equipped with a 60× supercorrected Plan Apo N

60XOSC objective (NA = 1.4, working distance = 0.12 mm) using mFV10-ASW software. Embryos were imaged in a custom chamber made of a 0.8-mm-thick metal slide with a 5-mm hole in the center and coverslips attached on both sides of the hole with a thin layer of vacuum grease, lightly compressing the embryo between the coverslips. Embryos were mounted in 0.1× MMR, and the imaging chamber was inverted to image the epithelial cells in the animal hemisphere at RT using the Olympus Fluoview 1000.

Live imaging of calcium and Rho flares was generally captured by scanning the top three apical Z-planes (step size of 0.5 μm) and acquired sequentially by line scanning to avoid bleed-through between channels. Global calcium (GCaMP6m), Rho flares, and ZO-1 were acquired at a 2-μs/pixel scanning speed, 5-s time interval, and 1.5–2× zoom. Local calcium (mNeon-PKC-β-C2), Rho flares, and membrane or ZO-1 were acquired at a 4-μs/pixel scanning speed, 10-s time interval, and 2× zoom. For ZnUMBA, eight apical Z-planes were acquired at an 8-μs/pixel scanning speed, 21-s time interval, and 1.5× zoom. For laser injury, three to four apical Z-planes were acquired at a 4–8-μs/pixel scanning speed with a 6-s time interval and 3× zoom.

Optogenetic stimulation and image acquisition

Whole-field stimulation

Simultaneous live imaging and optogenetic experiments were performed on the Olympus Fluoview 1000 microscope described above, using the Time Controller in the mFV10-ASW software. Time-lapse movies of prGEF-mCherry or active RhoA (mCherry-2xrGBD) were acquired with a 559-nm laser, scanning the three apical Z-planes (step size of 0.5 μm) at 8-μs/pixel scanning speed, 9-s time interval, and a 1× zoom for a total of 900 s. Simultaneous whole-field optogenetic stimulation was performed during live imaging by creating a 512 × 512-pixel region of interest (ROI) using 3% 405-nm laser power and the simultaneous (SIM) scanner to stimulate the ROI for a duration of 1 s with a 20-s interval between stimulations, for a total of 300 s. For Fig. S2 E, where we tested site-specific recruitment of prGEF-mCherry, a rectangle ROI encompassing the vertex-to-vertex length of a junction was stimulated as described for the whole-field ROI above, and time-lapse videos were acquired as described above.

Regional stimulation

Live imaging of active Rho (mCherry-2xrGBD) in embryos mosaicly injected with the optogenetic constructs was acquired with a 559-nm laser using the Time Controller device and scanning the three apical Z-planes (step size of 0.5 μm) at 8-μs/pixel scanning speed, 9-s time interval, and 1× zoom. Regional optogenetic stimulation of active RhoA was performed for 300 s by creating a rectangular ROI that encompassed one quarter of the field of view. A 3% 405-nm laser and the SIM scanner were used to stimulate the ROI for a duration of 1 s with a 20-s interval between stimulations, for a total of 900 s.

Site-specific stimulation

Live imaging of active Rho (mCherry-2xrGBD) or Halo-PKC-β-C2 (with Janelia Fluor 549 HaloTag Ligand) was acquired using

a 559-nm laser, scanning the three apical Z-planes (step size of 0.5 μm) at 8- μs /pixel scanning speed, 9-s time interval, and 3 \times zoom. Site-specific optogenetic stimulation was performed by drawing a rectangular ROI encompassing the vertex-to-vertex length of individual cell-cell junctions. A 5% 405-nm laser and the SIM scanner were used to stimulate the ROI for a duration of 1 s with a 10-s interval between stimulations, for a total of 180 s.

Laser injury of junctions

Laser injury was performed on the Olympus FV1000 microscope described above using a 405-nm laser and SIM scanner with the clip tornado function. A minimum of 10 frames were acquired before injury to establish a baseline. A small circular ROI corresponding to the width of the junction (0.4–0.6 μm in diameter) was placed roughly midway between two vertices. Injury was initiated manually by the user and was stopped by the software after 5 s of 100% laser power. For the majority of embryos, these conditions elicited local F-actin accumulation and junction contraction, as reported previously. In some cases (6 of 43 control embryos), laser injury resulted in a calcium spike that rapidly returned to baseline and was accompanied by global F-actin accumulation. In other cases (4 of 43 control embryos), repair was not initiated, and the break in the junction widened over the course of the video. These embryos were excluded from the analysis shown in Fig. 2 F.

Laser wounding of cell cortex

Laser wounding was performed on pigmented embryos using the Olympus FV1000 405-nm laser and SIM scanner with the clip tornado function. A minimum of 10 frames were acquired before wounding to establish a baseline. A circular ROI encompassing the junction and part of the cytoplasm (8.3 μm in diameter) was placed roughly midway between two vertices on the junction. Wounding was initiated manually by the user and was stopped by the software after 1.4 s of 40% laser power.

Drug treatments

The intracellular calcium chelator BAPTA-AM (15551; Cayman) and the IP₃R blocker 2-APB (D9754; Sigma-Aldrich) were resuspended in DMSO as a 20- or 25-mM stock, respectively, aliquoted, and stored at -20°C . Before treatment, the translucent vitelline envelope of gastrula-stage embryos was manually removed using sharp forceps on a dish coated with 1% low-melting-point agarose. The vitelline was grabbed with forceps and gently peeled starting from the vegetal pole of the embryo to avoid damage to the animal cap epithelium (Sive et al., 2007). Naked embryos were allowed to recover in 0.1 \times MMR for 30 min at 15°C . Following recovery, embryos were incubated for 1 h at 15°C before imaging in either 0.5% DMSO (vehicle) or a mixture of 20 μM BAPTA-AM and 100 μM 2-APB in 0.1 \times MMR.

The IP₃R blocker XeC (1280; Tocris) was resuspended in DMSO as a 1-mM stock, aliquoted, and stored at -20°C . Before treatment, XeC was diluted to a concentration of 125 μM in water, and a total of 10 nl was microinjected into the blastocoel of intact gastrula-stage embryos and incubated in the dark for 1 h at 15°C before imaging. For vehicle control, 10 nl of 1.25% DMSO was microinjected into the blastocoel of intact gastrula-

stage embryos and incubated in the dark for 1 h at 15°C before imaging.

The MSC blocker GsMTx4 (08GSM001; Smartox) was resuspended in water as a 500- μM stock, aliquoted, and stored at -20°C . Before use, GsMTx4 was diluted to a concentration of 25 μM in water and mixed with mRNA, and a total of 2 ng was microinjected into each embryo at the two- to four-cell stage.

Live imaging barrier assay

ZnUMBA was performed as previously reported (Stephenson et al., 2019). Briefly, gastrula-stage albino embryos expressing mCherry-2xrGBD and BFP-ZO-1 or BFP-PKC- β -C2 were microinjected into the blastocoel with 10 nl of 1 mM FluoZin-3 containing 100 μM CaCl₂ and 100 μM EDTA. FluoZin-3-injected embryos were allowed to recover from microinjection for 5 min in 0.1 \times MMR. After recovery, embryos were mounted in 0.1 \times MMR containing 1 mM ZnCl₂ and imaged immediately using confocal microscopy.

Immunofluorescence staining

Albino embryos injected with vehicle (water) or 12.5 μM GsMTx4 were fixed and immunostained for pMLC and F-actin as previously reported (Arnold et al., 2019). Briefly, gastrula-stage embryos were fixed overnight at RT with a mixture of 1.5% PFA, 0.25% glutaraldehyde, 0.2% Triton X-100, Alexa Fluor 647 phalloidin (1:1,000; #A22287; Thermo Fisher Scientific) in 0.88 \times MT buffer (80 mM K-Pipes, 5 mM EGTA, and 1 mM MgCl₂, pH 6.8 with KOH). Fixed embryos were quenched for 1 h at RT with 100 mM sodium borohydride in 1 \times PBS and blocked overnight in 10% FBS, 5% DMSO, and 0.1% NP-40 in 1 \times Tris-buffered Saline. Animal caps of the bisected embryos were incubated overnight at 4°C in rabbit anti-P-MLC (1:100; #3671; Cell Signaling Technologies) in blocking solution, washed three times with blocking solution, and incubated overnight at 4°C in goat anti-rabbit Alexa Fluor 488 IgG (1:200; #A11008; Thermo Fisher Scientific) and Alexa Fluor 647 phalloidin (1:1,000). Embryos were washed and mounted in VECTASHIELD (#101098-042; VWR) before imaging.

For E-cadherin staining, gastrula-stage embryos were fixed and immunostained using TCA fixative as reported previously (Reyes et al., 2014). Briefly, embryos were fixed for 1.5 h at RT in 2% TCA. Fixed embryos were washed three times with 1 \times PBS and bisected with a sharp scalpel to remove the vegetal hemisphere. Animal caps of the bisected embryos were permeabilized for 20 min at RT in a mix of 1% Triton X-100 in 1 \times PBS, followed by 20-min incubation in 1 \times PBST (0.1% Triton X-100 in 1 \times PBS). Permeabilized embryos were blocked overnight at 4°C in blocking solution (5% FBS in 1 \times PBST). After blocking, animal caps were incubated overnight at 4°C in mouse anti-E-Cadherin (1:1,000; #5D3-C; DSHB) in blocking solution, washed overnight in blocking solution, and incubated for 6 h at 4°C in goat anti-mouse Alexa Fluor 488 IgG (1:200; #A11001; Thermo Fisher Scientific) in blocking solution. Animal caps were stained for DNA using 10 $\mu\text{g}/\text{ml}$ DAPI (#D1306; Invitrogen) for 30 min at RT, washed, and mounted in VECTASHIELD (#101098-042; VWR) before imaging.

Image processing and quantification

Image processing and analysis were performed using ImageJ (Fiji). Sum intensity projections of the Z-series were used for all quantification, and confocal images of time-lapse videos represented in all figures are sum projections of three apical Z-planes (1.5 μm), with the exception of FluoZin-3 (eight apical Z-planes, 4 μm) and laser injury (three to four apical Z-planes, 1.8–2.4 μm). Sum intensity Z-projections of Fig. S4, C and D, were performed using QuickFigures, a plugin in ImageJ.

Quantification of calcium dynamics during Rho flares

Calcium dynamics at Rho flares were measured using a circular ROI of 2.5- μm diameter drawn at the site of flares, spanning the membrane and cytoplasm adjacent to the membrane, manually tracked over every frame to account for in-plane drifting in live tissue, and normalized to a baseline of 1. Cytosolic calcium (GCaMP6m) was calculated for each frame using the formula $F_{\text{normalized}} = (F/F_{\text{baseline}})$, where F_{baseline} represents the average calcium intensity of the first 150 s. Local calcium (PKC-C2) was calculated for each frame using the formula $F = (F_{\text{flare}} - F_{\text{background}})$ and normalized to a baseline of 1, where F_{baseline} represents the average calcium intensity of the first 100 s, and $F_{\text{background}}$ represents the cytoplasmic C2 intensity measured using an ROI of same size. An average of three independent measurements of calcium dynamics at each Rho flare was considered one data point ($n = 1$).

For accurate measurement of calcium flash dynamics using the cytoplasmic soluble calcium probe (GCaMP6m), Rho flares were selected from cells that exhibited an isolated Rho flare that was not interrupted by a multicellular traveling calcium wave for 500 s before and after the initiation of Rho flares.

Intensity and duration of Rho flares and ZO-1 were measured at the site of Rho flares using a small circular ROI (GCaMP6m, 0.8 μm ; PKC-C2, 2.5 μm ; and FluoZin-3, 2.2 μm) and normalized to a nearby reference junction without Rho flares using ROIs of the same size to account for photobleaching and drifting in the Z-plane. With the exception of Fig. 4, the frame before the rapid increase in Rho activity was assigned as the start of the Rho flare and aligned to time 0 s in the graphs. The rapid increase in Rho activity was defined as a 5% increase in normalized active Rho intensity for at least three of four consecutive frames (Stephenson et al., 2019). For Fig. 4, as calcium chelation (BAPTA-AM + 2-APB) significantly reduced the intensity of Rho flares, we adopted an alternative method to align time 0 s in the graph to the frame before the rapid decrease in ZO-1; the decrease in ZO-1 was defined as a 5% decrease in normalized ZO-1 intensity for at least three of four consecutive frames.

Optogenetic whole-field stimulation quantification

Multiple 0.7- μm circular ROIs were placed on randomly selected junctions and were moved manually to compensate for lateral drift of the embryos. Measurements of LOVpep, prGEF, and active Rho were taken three times for each junction and averaged. Each time point was normalized by dividing by the average of the first 300 s to set a baseline of 1.

Optogenetic regional stimulation quantification

Rho flare frequency was measured manually by counting the number of flare occurrences at cell-cell junctions only in the

“region of observation” (not the region that was optogenetically stimulated). Rho flares included in the analysis were only those that initiated during 0–300 s (pre-stimulation) or 600–900 s (post-stimulation).

Optogenetic site-specific stimulation quantification

A 0.7- μm circular ROI was placed on stimulated junctions for both active Rho and Halo-PKC- β -C2 experiments and was moved manually to compensate for lateral drift. Measurements were taken in triplicate and then averaged. Each data point was normalized by dividing by the average of the first 60 s to set a baseline of 1.

Quantification of laser injury

An ROI 6 μm in diameter was used to measure the intensity of Lifeact-GFP and R-GECO1 at the site of the injury and a reference junction. ROIs were moved manually to correct for lateral movement of the tissue. Because R-GECO1 intensity increases throughout the cell after injury, reference junctions were chosen such that they did not belong to either of the injured cells. Note: during injury, R-GECO1 increases in intensity throughout the whole field of view, but the change is sustained only in injured cells. To calculate the normalized intensity, the mean intensity of the injury ROI was divided by the mean intensity of the reference ROI. Measurements were aligned by the frame at which injury occurred, and the baseline was normalized to 1 by dividing each time point by the average of the 10 time points before injury.

Propagation of calcium wave during laser wounding

Intensity and propagation of calcium wave were measured by dividing the field of view (212 \times 132 μm) into three regions, with region 1 being the region encompassing the cells subjected to laser wounding. Intensity of calcium was measured in all three regions over time and normalized to calcium intensity 30 s before wounding in the respective regions.

Duration of calcium flash

Duration of the calcium flash was quantified by measuring the full duration at half-maximum (FDHM) of the individual normalized calcium flashes at sites of Rho flares. FDHM (seconds) was measured manually by calculating the duration at 50% of the maximum amplitude above the baseline of 1 on the ascent and descent of the calcium transient. Experiments in which calcium increased less than twofold over the baseline were eliminated from the analysis. FDHM was plotted in a scatter plot.

Area under the curve (AUC)

AUC for active Rho flares and calcium flashes was quantified using GraphPad Prism 9.0 by applying AUC analysis of the individual traces. AUC analysis was applied to all points in the peaks above the baseline of 1, and peaks <10% of the increase from the baseline to the maximum Y-value were ignored. Individual AUC values for each Rho flare or calcium flash were plotted in a scatter plot.

Correlation coefficient

Intensity of active Rho and calcium for individual flares was measured manually using the polygon area selection tool in

ImageJ. The area of an individual Rho flare was measured to find the maximum size of the flare. At the maximum size of the Rho flare, intensity of calcium and intensity of active RhoA were measured at the protrusion for a total of 25 s (2 frames before the maximum size, at its maximum size, and 2 frames after the maximum size). The average intensity of active RhoA was plotted against the intensity of calcium for individual flares on a correlation plot and fitted with a line of best fit, and the Pearson correlation coefficient was calculated using GraphPad Prism.

Frequency of Rho flares

Rho flare frequency was measured manually using ImageJ, by counting the number of Rho flare occurrences at cell–cell junctions in the whole field of imaging from the start of the time-lapse movie. Rho flares in which the local active RhoA intensity increased and was sustained at the junctions for a span of ~80–100 s were included in the analysis.

Global barrier function

Global barrier function was quantified by measuring the whole field intensity of FluoZin-3 signal, including junctional and cytoplasmic, over time using an ROI of $141.12 \times 141.12 \mu\text{m}$. Time 0 s represents the start of image acquisition, which began immediately following mounting of the embryo injected with FluoZin-3 in $0.1\times$ MMR containing 1 mM ZnCl_2 . Each timepoint was measured, and baseline was normalized to 1 by dividing the individual value by the average of the first 84 s.

Junction length

The length of the cell–cell junction was quantified using ZO-1 as junctional marker. Using ImageJ, a $0.3\text{-}\mu\text{m}$ -wide segmented line was drawn on junctions with Rho flares to trace the junction from vertex to vertex. The length of the line was measured for every other frame by manually advancing and adjusting the line to accommodate cell shape changes through the time-lapse video. Each junction was measured in triplicate, and change in length was calculated by subtracting the individual values from the average of the first 60 s.

Construction of kymographs

Kymographs from vertex-to-vertex of a cell–cell junction were constructed by digitizing cell–cell junctions using ZO-1 as junctional marker. Each horizontal line in the kymograph was generated by measuring the intensity of ZO-1 and active Rho using $0.75\text{-}\mu\text{m}$ circular ROIs positioned at points along the length of the cell–cell junction. Kymographs were constructed by stacking and center aligning the horizontal lines from successive time frames (Stephenson et al., 2019).

Apical cell perimeter

The apical perimeter of the cell was quantified using ZO-1 to identify cell boundaries. Using ImageJ, a segmented line was drawn to trace the boundary of the cells with a calcium flash and neighboring cells without a calcium flash over time. The perimeter of the cell was measured for every time point by manually adjusting the line to accommodate cell shape changes. Change in apical perimeter was calculated by subtracting the

current perimeter from the initial perimeter (average perimeter over the first three time points).

Intensity of F-actin and P-MLC

Junctional and cytoplasmic intensity of F-actin and P-MLC were quantified in ImageJ. Junctional intensity was measured using a $2.07\text{-}\mu\text{m}$ -wide segmented line to trace a bicellular junction (excluding vertices), and the matched cytoplasmic intensity was measured using a $10.4\text{-}\mu\text{m}$ circular ROI. Ratio of junctional/cytoplasmic F-actin or P-MLC was calculated by dividing the intensity at the junction by the intensity in the cytoplasm for each cell.

Intensity of E-cadherin

Junctional and cytoplasmic intensity of E-cadherin was quantified in ImageJ. Intensity was measured using a $1.03\text{-}\mu\text{m}$ -wide segmented line to trace a bicellular junction (excluding vertices), and background cytoplasmic intensity was measured using the same $1.03\text{-}\mu\text{m}$ -wide segmented line. Ratio of junctional/cytoplasmic E-Cadherin was calculated by dividing the intensity at the junction by the intensity in the cytoplasm for each junction.

Statistical analysis

Statistical analysis and SEM were calculated in GraphPad Prism 9.0. Data distribution was assumed to be normal but was not formally tested. Statistical analysis between two groups was measured using a two-tailed, unpaired Mann–Whitney *U* test, with the exception of flare frequency and intensity of actomyosin. The statistical significance of frequency of Rho flares was measured using a two-tailed, paired Student's *t* test. Statistical significance of F-actin and P-MLC intensity at the junctions and the junction/cytoplasm ratio was measured using a one-way ANOVA.

Online supplemental material

Five supplemental figures and 10 videos are included illustrating the dynamics of calcium, active Rho, and ZO-1 during TJ remodeling. Fig. S1 shows different calcium dynamics in the gastrula-stage *Xenopus* epithelium. Fig. S2 shows whole-field and site-specific stimulation of active RhoA using optogenetics. Fig. S3 shows the effect of blocking IP_3R -mediated calcium release from the ER on calcium dynamics and F-actin accumulation. Fig. S4 shows the effect of GsMTx4 on cell–cell junctions and baseline active RhoA. Fig. S5 shows the effect of GsMTx4 on dynamics of Rho flares and junction contraction. Videos 1 and 2 show local calcium increase at sites of leaks and Rho flares. Video 3 shows naturally occurring calcium flashes and calcium waves. Video 4 shows a calcium flash at the site of ZO-1 loss and Rho flares. Video 5 shows a calcium flash and F-actin accumulation at the site of laser-induced TJ loss. Video 6 shows whole-field recruitment of prGEF and activation of RhoA using optogenetics. Video 7 shows the effect of junction-specific activation of RhoA on calcium flashes. Video 8 shows ZO-1 breaks and Rho flares in intracellular calcium chelated cells. Video 9 shows the frequency of Rho flares in vehicle- and GsMTx4-treated embryos. Video 10 shows repeating local FluoZin-3 increase and Rho flares in GsMTx4-treated embryos vs. vehicle-treated embryos.

Acknowledgments

We thank W.M. Bement for pCS2+/mCherry-2xrGBD, pCS2+/eGFP-PKC- β -C2, and pCS2+/R-GECO1 constructs; P.W. Oakes for the Stargazin-GFPsient-LOVpep construct and expert advice on optogenetics; and L. van den Goor for the pCS2+/N-Halo-tag construct. We also thank all current and former members of the A.L. Miller laboratory for providing helpful discussion and feedback on experiments.

This work was supported by a National Institutes of Health grant (2R01 GM112794) to A.L. Miller, a predoctoral fellowship from the American Heart Association (20PRE35120588) to S. Varadarajan, a National Science Foundation Graduate Research Fellowship to S.A. Chumki, and Biotechnology and Biological Sciences Research Council grants BB/P01190X and BB/P006507 to A.B. Goryachev.

The authors declare no competing financial interests.

Author contributions: S. Varadarajan and A.L. Miller conceptualized the study; S. Varadarajan, R.E. Stephenson, S.A. Chumki, and A.L. Miller developed the methodology; S. Varadarajan performed the majority of experiments and data analysis; S.A. Chumki performed experiments and analyzed data for Figs. 3, 5, and S2; R.E. Stephenson performed experiments and analyzed data for Fig. 2 (E and F) and Fig. S1 (G and G') and analyzed data for Fig. S3 D; J.L. Wu performed the experiment and analyzed data for Fig. S4 (C-C"); E.R. Misterovich analyzed the data for Fig. 5 A and Fig. 7 (F and F'); C.E. Dudley optimized the expression level and dye concentration for using Halo-tag constructs in *Xenopus* embryos; I.S. Erofeev constructed the kymographs for Fig. 7 G; S. Varadarajan, S.A. Chumki, R.E. Stephenson, and A.L. Miller wrote the original draft of the manuscript; all authors revised the manuscript; A.L. Miller and A.B. Goryachev acquired funding; A.L. Miller supervised the study.

Submitted: 18 May 2021

Revised: 3 December 2021

Accepted: 2 February 2022

References

Acharya, B.R., A. Nestor-Bergmann, X. Liang, S. Gupta, K. Duszyc, E. Gaudeloin, G.A. Gomez, S. Budnar, P. Marcq, O.E. Jensen, et al. 2018. A mechanosensitive RhoA pathway that protects epithelia against acute tensile stress. *Dev. Cell.* 47:439–452.e6. <https://doi.org/10.1016/j.devcel.2018.09.016>

Akazawa, Y., T. Yuki, H. Yoshida, Y. Sugiyama, and S. Inoue. 2013. Activation of TRPV4 strengthens the tight-junction barrier in human epidermal keratinocytes. *Skin Pharmacol. Physiol.* 26:15–21. <https://doi.org/10.1159/000343173>

Arnold, T.R., J.H. Shawky, R.E. Stephenson, K.M. Dinshaw, T. Higashi, F. Huq, L.A. Davidson, and A.L. Miller. 2019. Anillin regulates epithelial cell mechanics by structuring the medial-apical actomyosin network. *Elife.* 8:e39065. <https://doi.org/10.7554/eLife.39065>

Bae, C., F. Sachs, and P.A. Gottlieb. 2011. The mechanosensitive ion channel Piezo1 is inhibited by the peptide GsMTx4. *Biochemistry.* 50:6295–6300. <https://doi.org/10.1021/bi200770q>

Balaji, R., C. Biemeier, H. Harz, J. Bates, C. Stadler, A. Hildebrand, and A.-K. Classen. 2017. Calcium spikes, waves and oscillations in a large, patterned epithelial tissue. *Sci. Rep.* 7:42786. <https://doi.org/10.1038/srep42786>

Benink, H.A., and W.M. Bement. 2005. Concentric zones of active RhoA and Cdc42 around single cell wounds. *J. Cell Biol.* 168:429–439. <https://doi.org/10.1083/jcb.200411109>

Berridge, M.J. 2006. Calcium microdomains: Organization and function. *Cell Calcium* 40:405–412. <https://doi.org/10.1016/j.ceca.2006.09.002>

Bowman, C.L., P.A. Gottlieb, T.M. Suchyna, Y.K. Murphy, and F. Sachs. 2007. Mechanosensitive ion channels and the peptide inhibitor GsMTx-4: History, properties, mechanisms and pharmacology. *Toxicol.* 49:249–270. <https://doi.org/10.1016/j.toxicol.2006.09.030>

Brodskiy, P.A., and J.J. Zartman. 2018. Calcium as a signal integrator in developing epithelial tissues. *Phys. Biol.* 15:051001. <https://doi.org/10.1088/1478-3975/aabb18>

Budnar, S., K.B. Husain, G.A. Gomez, M. Naghibosadat, A. Varma, S. Verma, N.A. Hamilton, R.G. Morris, and A.S. Yap. 2019. Anillin promotes cell contractility by cyclic resetting of RhoA residence kinetics. *Dev. Cell.* 49:894–906.e812. <https://doi.org/10.1016/j.devcel.2019.04.031>

Cavanaugh, K.J., T.S. Cohen, and S.S. Margulies. 2006. Stretch increases alveolar epithelial permeability to uncharged micromolecules. *Am. J. Physiol. Cell Physiol.* 290:C1179–C1188. <https://doi.org/10.1152/ajpcell.00355.2004>

Charras, G.T. 2008. A short history of blebbing. *J. Microsc.* 231:466–478. <https://doi.org/10.1111/j.1365-2818.2008.02059.x>

Chen, T.W., T.J. Wardill, Y. Sun, S.R. Pulver, S.L. Renninger, A. Baohan, E.R. Schreiter, R.A. Kerr, M.B. Orger, V. Jayaraman, et al. 2013. Ultrasensitive fluorescent proteins for imaging neuronal activity. *Nature.* 499:295–300. <https://doi.org/10.1038/nature12354>

Cho, W., and R.V. Stahelin. 2006. Membrane binding and subcellular targeting of C2 domains. *Biochim. Biophys. Acta Mol. Cell Biol. Lipids.* 1761:838–849. <https://doi.org/10.1016/j.bbalip.2006.06.014>

Christodoulou, N., and P.A. Skourides. 2015. Cell-autonomous Ca²⁺ flashes elicit pulsed contractions of an apical actin network to drive apical constriction during neural tube closure. *Cell Rep.* 13:2189–2202. <https://doi.org/10.1016/j.celrep.2015.11.017>

Clark, A.G., A.L. Miller, E. Vaughan, H.Y.E. Yu, R. Penkert, and W.M. Bement. 2009. Integration of single and multicellular wound responses. *Curr. Biol.* 19:1389–1395. <https://doi.org/10.1016/j.cub.2009.06.044>

Claude, P., and D.A. Goodenough. 1973. Fracture faces of zonulae occludentes from "tight" and "leaky" epithelia. *J. Cell Biol.* 58:390–400. <https://doi.org/10.1083/jcb.58.2.390>

Cohen, T.S., K.J. Cavanaugh, and S.S. Margulies. 2008. Frequency and peak stretch magnitude affect alveolar epithelial permeability. *Eur. Respir. J.* 32:854–861. <https://doi.org/10.1183/09031936.00141007>

Coste, B., J. Mathur, M. Schmidt, T.J. Earley, S. Ranade, M.J. Petrus, A.E. Dubin, and A. Patapoutian. 2010. Piezo1 and Piezo2 are essential components of distinct mechanically activated cation channels. *Science.* 330:55–60. <https://doi.org/10.1126/science.1193270>

Davenport, N.R., K.J. Sonnemann, K.W. Eliceiri, and W.M. Bement. 2016. Membrane dynamics during cellular wound repair. *Mol. Biology Cell.* 27:2272–2285. <https://doi.org/10.1091/mbc.E16-04-0223>

Denker, B.M., and S.K. Nigam. 1998. Molecular structure and assembly of the tight junction. *Am. J. Physiol.* 274:F1–F9. <https://doi.org/10.1152/ajprenal.1998.274.1.F1>

Elamin, E., A. Masclee, J. Dekker, and D. Jonkers. 2014. Ethanol disrupts intestinal epithelial tight junction integrity through intracellular calcium-mediated Rho/ROCK activation. *Am. J. Physiol. Gastrointest. Liver Physiol.* 306:G677–G685. <https://doi.org/10.1152/ajpgi.00236.2013>

Ellefsen, K.L., J.R. Holt, A.C. Chang, J.L. Nourse, J. Arulmoli, A.H. Mekhdjian, H. Abuwarda, F. Tombola, L.A. Flanagan, A.R. Dunn, et al. 2019. Myosin-II mediated traction forces evoke localized Piezo1-dependent Ca²⁺ flickers. *Commun. Biol.* 2:298. <https://doi.org/10.1038/s42003-019-0514-3>

Fanning, A.S., B.J. Jameson, L.A. Jesaitis, and J.M. Anderson. 1998. The tight junction protein ZO-1 establishes a link between the transmembrane protein occludin and the actin cytoskeleton. *J. Biol. Chem.* 273:29745–29753. <https://doi.org/10.1074/jbc.273.45.29745>

Furuse, M., H. Sasaki, K. Fujimoto, and S. Tsukita. 1998. A single gene product, claudin-1 or -2, reconstitutes tight junction strands and recruits occludin in fibroblasts. *J. Cell Biol.* 143:391–401. <https://doi.org/10.1083/jcb.143.2.391>

Gnanasambandam, R., C. Ghatak, A. Yasmann, K. Nishizawa, F. Sachs, A.S. Ladokhin, S.I. Sukharev, and T.M. Suchyna. 2017. GsMTx4: Mechanism of inhibiting mechanosensitive ion channels. *Biophys. J.* 112:31–45. <https://doi.org/10.1016/j.bpj.2016.11.013>

Gonzalez-Mariscal, L., R.G. Contreras, J.J. Bolivar, A. Ponce, B. Chavez De Ramirez, and M. Cerejido. 1990. Role of calcium in tight junction formation between epithelial cells. *Am. J. Physiol.* 259:C978–C986. <https://doi.org/10.1152/ajpcell.1990.259.6.C978>

Gudipaty, S.A., J. Lindblom, P.D. Loftus, M.J. Redd, K. Edes, C.F. Davey, V. Krishnegowda, and J. Rosenblatt. 2017. Mechanical stretch triggers

- rapid epithelial cell division through Piezo1. *Nature*. 543:118–121. <https://doi.org/10.1038/nature21407>
- Gudipaty, S.A., and J. Rosenblatt. 2016. Epithelial cell extrusion: Pathways and pathologies. *Semin. Cell Dev. Biol.* 67:132–140. <https://doi.org/10.1016/j.semcdb.2016.05.010>
- Guillot, C., and T. Lecuit. 2013. Mechanics of epithelial tissue homeostasis and morphogenesis. *Science*. 340:1185–1189. <https://doi.org/10.1126/science.1235249>
- Heisenberg, C.-P. 2017. Cell biology: Stretched divisions. *Nature*. 543:43–44. <https://doi.org/10.1038/nature21502>
- Heissler, S.M., and J.R. Sellers. 2014. Myosin light chains: Teaching old dogs new tricks. *Bioarchitecture*. 4:169–188. <https://doi.org/10.1080/19490992.2015.1054092>
- Higashi, T., T.R. Arnold, R.E. Stephenson, K.M. Dinshaw, and A.L. Miller. 2016. Maintenance of the epithelial barrier and remodeling of cell–cell junctions during cytokinesis. *Curr. Biol.* 26:1829–1842. <https://doi.org/10.1016/j.cub.2016.05.036>
- Holinstat, M., D. Mehta, T. Kozasa, R.D. Minshall, and A.B. Malik. 2003. Protein kinase Calpha-induced p115RhoGEF phosphorylation signals endothelial cytoskeletal rearrangement. *J. Biol. Chem.* 278:28793–28798. <https://doi.org/10.1074/jbc.M303900200>
- Hunter, G.L., J.M. Crawford, J.Z. Genkins, and D.P. Kiehart. 2014. Ion channels contribute to the regulation of cell sheet forces during *Drosophila* dorsal closure. *Development*. 141:325–334. <https://doi.org/10.1242/dev.097097>
- Inaba, H., Q. Miao, and T. Nakata. 2021. Optogenetic control of small GTPases reveals RhoA mediates intracellular calcium signaling. *J. Biol. Chem.* 296:100290. <https://doi.org/10.1016/j.jbc.2021.100290>
- Itoh, M., M. Furuse, K. Morita, K. Kubota, M. Saitou, and S. Tsukita. 1999. Direct binding of three tight junction-associated MAGUKs, ZO-1, ZO-2, and ZO-3, with the COOH termini of claudins. *J. Cell Biol.* 147:1351–1363. <https://doi.org/10.1083/jcb.147.6.1351>
- Ivanov, A.I., C.A. Parkos, and A. Nusrat. 2010. Cytoskeletal regulation of epithelial barrier function during inflammation. *Am. J. Pathol.* 177:512–524. <https://doi.org/10.2353/ajpath.2010.100168>
- Jaffe, L.F. 2008. Calcium waves. *Philos. Trans. R. Soc. Lond. B Biol. Sci.* 363:1311–1316. <https://doi.org/10.1098/rstb.2007.2249>
- Liu, C., and C. Montell. 2015. Forcing open TRP channels: Mechanical gating as a unifying activation mechanism. *Biochem. Biophys. Res. Commun.* 460:22–25. <https://doi.org/10.1016/j.bbrc.2015.02.067>
- Luissint, A.C., C.A. Parkos, and A. Nusrat. 2016. Inflammation and the intestinal barrier: Leukocyte-epithelial cell interactions, cell junction remodeling, and mucosal repair. *Gastroenterology*. 151:616–632. <https://doi.org/10.1053/j.gastro.2016.07.008>
- Marchiando, A.M., W.V. Graham, and J.R. Turner. 2010. Epithelial barriers in homeostasis and disease. *Annu. Rev. Pathol.* 5:119–144. <https://doi.org/10.1146/annurev.pathol.4.110807.092135>
- Miller, A.L., and W.M. Bement. 2009. Regulation of cytokinesis by Rho GTPase flux. *Nat. Cell Biol.* 11:71–77. <https://doi.org/10.1038/ncb1814>
- Miyamoto, T., T. Mochizuki, H. Nakagomi, S. Kira, M. Watanabe, Y. Takayama, Y. Suzuki, S. Koizumi, M. Takeda, and M. Tominaga. 2014. Functional role for Piezo1 in stretch-evoked Ca²⁺ influx and ATP release in Urothelial cell cultures. *J. Biol. Chem.* 289:16565–16575. <https://doi.org/10.1074/jbc.M113.528638>
- Mochizuki, T., T. Sokabe, I. Araki, K. Fujishita, K. Shibasaki, K. Uchida, K. Naruse, S. Koizumi, M. Takeda, and M. Tominaga. 2009. The TRPV4 cation channel mediates stretch-evoked Ca²⁺ influx and ATP release in primary urothelial cell cultures. *J. Biol. Chem.* 284:21257–21264. <https://doi.org/10.1074/jbc.M109.020206>
- Moriwaki, K., S. Tsukita, and M. Furuse. 2007. Tight junctions containing claudin 4 and 6 are essential for blastocyst formation in preimplantation mouse embryos. *Dev. Biol.* 312:509–522. <https://doi.org/10.1016/j.ydbio.2007.09.049>
- Murakoshi, H., H. Wang, and R. Yasuda. 2011. Local, persistent activation of Rho GTPases during plasticity of single dendritic spines. *Nature*. 472:100–104. <https://doi.org/10.1038/nature09823>
- Nigam, S.K., E. Rodriguez-Boulan, and R.B. Silver. 1992. Changes in intracellular calcium during the development of epithelial polarity and junctions. *Proc. Natl. Acad. Sci. USA*. 89:6162–6166. <https://doi.org/10.1073/pnas.89.13.6162>
- Nourse, J.L., and M.M. Pathak. 2017. How cells channel their stress: Interplay between Piezo1 and the cytoskeleton. *Semin. Cell Dev. Biol.* 71:3–12. <https://doi.org/10.1016/j.semcdb.2017.06.018>
- Nusrat, A., M. Giry, J.R. Turner, S.P. Colgan, C.A. Parkos, D. Carnes, E. Lemichez, P. Boquet, and J.L. Madara. 1995. Rho protein regulates tight junctions and perijunctional actin organization in polarized epithelia. *Proc. Natl. Acad. Sci. USA*. 92:10629–10633. <https://doi.org/10.1073/pnas.92.23.10629>
- Oakes, P.W., E. Wagner, C.A. Brand, D. Probst, M. Linke, U.S. Schwarz, M. Glotzer, and M.L. Gardel. 2017. Optogenetic control of RhoA reveals zyxin-mediated elasticity of stress fibres. *Nat. Commun.* 8:15817. <https://doi.org/10.1038/ncomms15817>
- Orr, A.W., B.P. Helmke, B.R. Blackman, and M.A. Schwartz. 2006. Mechanisms of mechanotransduction. *Dev. Cell*. 10:11–20. <https://doi.org/10.1016/j.devcel.2005.12.006>
- Pardo-Pastor, C., F. Rubio-Moscardo, M. Vogel-González, S.A. Serra, A. Afthinos, S. Mrkonjic, O. Destaing, J.F. Abenza, J.M. Fernández-Fernández, X. Trepal, et al. 2018. Piezo2 channel regulates RhoA and actin cytoskeleton to promote cell mechanobiological responses. *Proc. Natl. Acad. Sci. USA*. 115:1925–1930. <https://doi.org/10.1073/pnas.1718177115>
- Reyes, C.C., M. Jin, E.B. Breznau, R. Espino, R. Delgado-Gonzalo, A.B. Goryachev, and A.L. Miller. 2014. Anillin regulates cell–cell junction integrity by organizing junctional accumulation of Rho-GTP and actomyosin. *Curr. Biol.* 24:1263–1270. <https://doi.org/10.1016/j.cub.2014.04.021>
- Rosenblatt, J., M.C. Raff, and L.P. Cramer. 2001. An epithelial cell destined for apoptosis signals its neighbors to extrude it by an actin- and myosin-dependent mechanism. *Curr. Biol.* 11:1847–1857. [https://doi.org/10.1016/S0960-9822\(01\)00587-5](https://doi.org/10.1016/S0960-9822(01)00587-5)
- Sahu, S.U., M.R. Visetsouk, R.J. Garde, L. Hennes, C. Kwas, and J.H. Gutzman. 2017. Calcium signals drive cell shape changes during zebrafish midbrain–hindbrain boundary formation. *Mol. Biol. Cell*. 28:875–882. <https://doi.org/10.1091/mbc.E16-08-0561>
- Samak, G., T. Suzuki, A. Bhargava, and R.K. Rao. 2010. c-Jun NH2-terminal kinase-2 mediates osmotic stress-induced tight junction disruption in the intestinal epithelium. *Am. J. Physiol. Gastrointest. Liver Physiol.* 299:G572–G584. <https://doi.org/10.1152/ajpgi.00265.2010>
- Saoudi, Y., B. Rouseau, J. Doussiere, S. Charrasse, C. Gauthier-Rouviere, N. Morin, C. Sautet-Laugier, E. Denarier, R. Scaife, C. Mioskowski, and D. Job. 2004. Calcium-independent cytoskeleton disassembly induced by BAPTA. *Eur. J. Biochem.* 271:3255–3264. <https://doi.org/10.1111/j.1432-1033.2004.04259.x>
- Shao, X., Q. Li, A. Mogilner, A.D. Bershadsky, and G.V. Shivashankar. 2015. Mechanical stimulation induces formin-dependent assembly of a perinuclear actin rim. *Proc. Natl. Acad. Sci. USA*. 112:E2595–E2601. <https://doi.org/10.1073/pnas.1504837112>
- Shi, Z., Z.T. Graber, T. Baumgart, H.A. Stone, and A.E. Cohen. 2018. Cell membranes resist flow. *Cell*. 175:1769–1779.e13. <https://doi.org/10.1016/j.cell.2018.09.054>
- Sive, H.L., R.M. Grainger, and R.M. Harland. 2007. Removing the vitelline membrane from *Xenopus laevis* embryos. *CSH Protoc.* 2007:pdb prot4732. <https://doi.org/10.1101/pdb.prot4732>
- Sokabe, T., T. Fukumi-Tominaga, S. Yonemura, A. Mizuno, and M. Tominaga. 2010. The TRPV4 channel contributes to intercellular junction formation in keratinocytes. *J. Biol. Chem.* 285:18749–18758. <https://doi.org/10.1074/jbc.M110.103606>
- Soto, X., J. Li, R. Lea, E. Dubaissi, N. Papalopulu, and E. Amaya. 2013. Inositol kinase and its product accelerate wound healing by modulating calcium levels, Rho GTPases, and F-actin assembly. *Proc. Natl. Acad. Sci. USA*. 110:11029–11034. <https://doi.org/10.1073/pnas.1217308110>
- Spassova, M.A., T. Hewavitharana, W. Xu, J. Soboloff, and D.L. Gill. 2006. A common mechanism underlies stretch activation and receptor activation of TRPC6 channels. *Proc. Natl. Acad. Sci. USA*. 103:16586–16591. <https://doi.org/10.1073/pnas.0606894103>
- Staehelein, L.A., T.M. Mukherjee, and A.W. Williams. 1969. Freeze-etch appearance of the tight junctions in the epithelium of small and large intestine of mice. *Protoplasma*. 67:165–184. <https://doi.org/10.1007/BF01248737>
- Stephenson, R.E., T. Higashi, I.S. Erofeev, T.R. Arnold, M. Leda, A.B. Goryachev, and A.L. Miller. 2019. Rho flares repair local tight junction leaks. *Dev. Cell*. 48:445–459.e5. <https://doi.org/10.1016/j.devcel.2019.01.016>
- Strickland, D., Y. Lin, E. Wagner, C.M. Hope, J. Zayner, C. Antoniou, T.R. Sosnick, E.L. Weiss, and M. Glotzer. 2012. TULIPs: Tunable, light-controlled interacting protein tags for cell biology. *Nat. Methods*. 9:379–384. <https://doi.org/10.1038/nmeth.1904>
- Stuart, R.O., A. Sun, M. Panichas, S.C. Hebert, B.M. Brenner, and S.K. Nigam. 1994. Critical role for intracellular calcium in tight junction biogenesis. *J. Cell Physiol.* 159:423–433. <https://doi.org/10.1002/jcp.1041590306>
- Sun, L., R. Guan, I.J. Lee, Y. Liu, M. Chen, J. Wang, J.Q. Wu, and Z. Chen. 2015. Mechanistic insights into the anchorage of the contractile ring by

- anillin and Mid1. *Dev. Cell.* 33:413–426. <https://doi.org/10.1016/j.devcel.2015.03.003>
- Suzuki, M., M. Sato, H. Koyama, Y. Hara, K. Hayashi, N. Yasue, H. Imamura, T. Fujimori, T. Nagai, R.E. Campbell, and N. Ueno. 2017. Distinct intracellular Ca²⁺ dynamics regulate apical constriction and differentially contribute to neural tube closure. *Development.* 144:1307–1316. <https://doi.org/10.1242/dev.141952>
- Taha, A.A., M. Taha, J. Seebach, and H.J. Schnittler. 2014. ARP2/3-mediated junction-associated lamellipodia control VE-cadherin-based cell junction dynamics and maintain monolayer integrity. *Mol. Biol. Cell.* 25: 245–256. <https://doi.org/10.1091/mbc.e13-07-0404>
- Takeuchi, Y., R. Narumi, R. Akiyama, E. Vitiello, T. Shirai, N. Tanimura, K. Kuromiya, S. Ishikawa, M. Kajita, M. Tada, et al. 2020. Calcium wave promotes cell extrusion. *Curr. Biol.* 30:670–681.e6. <https://doi.org/10.1016/j.cub.2019.11.089>
- Tinevez, J.-Y., U. Schulze, G. Salbreux, J. Roensch, J.-F. Joanny, and E. Paluch. 2009. Role of cortical tension in bleb growth. *Proc. Natl. Acad. Sci. USA.* 106:18581–18586. <https://doi.org/10.1073/pnas.0903353106>
- Tirupathi, C., G.U. Ahmmmed, S.M. Vogel, and A.B. Malik. 2006. Ca²⁺ signaling, TRP channels, and endothelial permeability. *Microcirculation.* 13: 693–708. <https://doi.org/10.1080/10739680600930347>
- Tsai, F.C., G.H. Kuo, S.W. Chang, and P.J. Tsai. 2015. Ca²⁺ signaling in cytoskeletal reorganization, cell migration, and cancer metastasis. *BioMed Res. Int.* 2015:409245. <https://doi.org/10.1155/2015/409245>
- Van Itallie, C.M., A.J. Tietgens, and J.M. Anderson. 2017. Visualizing the dynamic coupling of claudin strands to the actin cytoskeleton through ZO-1. *Mol. Biol. Cell.* 28:524–534. <https://doi.org/10.1091/mbc.E16-10-0698>
- Varadarajan, S., R.E. Stephenson, and A.L. Miller. 2019. Multiscale dynamics of tight junction remodeling. *J. Cell Sci.* 132:jcs.229286. <https://doi.org/10.1242/jcs.229286>
- Wagner, E., and M. Glotzer. 2016. Local RhoA activation induces cytokinetic furrows independent of spindle position and cell cycle stage. *J. Cell Biol.* 213:641–649. <https://doi.org/10.1083/jcb.201603025>
- Wallingford, J.B., A.J. Ewald, R.M. Harland, and S.E. Fraser. 2001. Calcium signaling during convergent extension in *Xenopus*. *Curr. Biol.* 11:652–661. [https://doi.org/10.1016/s0960-9822\(01\)00201-9](https://doi.org/10.1016/s0960-9822(01)00201-9)
- Wang, J., and D.A. Richards. 2012. Segregation of PIP2 and PIP3 into distinct nanoscale regions within the plasma membrane. *Biol. Open.* 1:857–862. <https://doi.org/10.1242/bio.20122071>
- Webb, S.E., and A.L. Miller. 2006. Ca²⁺ signaling and early embryonic patterning during the Blastula and Gastrula Periods of Zebrafish and *Xenopus* development. *Biochim. Biophys. Acta Mol. Cell Res.* 1763: 1192–1208. <https://doi.org/10.1016/j.bbamcr.2006.08.004>
- Weber, E.W., and W.A. Muller. 2017. Roles of transient receptor potential channels in regulation of vascular and epithelial barriers. *Tissue Barriers.* 5:e1331722. <https://doi.org/10.1080/21688370.2017.1331722>
- Wei, C., X. Wang, M. Chen, K. Ouyang, L.S. Song, and H. Cheng. 2009. Calcium flickers steer cell migration. *Nature.* 457:901–905. <https://doi.org/10.1038/nature07577>
- Welf, E.S., C.E. Miles, J. Huh, E. Sapoznik, J. Chi, M.K. Driscoll, T. Isogai, J. Noh, A.D. Weems, T. Pohlkamp, et al. 2020. Actin-membrane release initiates cell protrusions. *Dev. Cell.* 55:723–736.e8. <https://doi.org/10.1016/j.devcel.2020.11.024>
- Woolner, S., A.L. Miller, and W.M. Bement. 2009. Imaging the cytoskeleton in live *Xenopus laevis* embryos. *Methods Mol. Biol.* 586:23–39. https://doi.org/10.1007/978-1-60761-376-3_2
- Yu, D., A.M. Marchiando, C.R. Weber, D.R. Raleigh, Y. Wang, L. Shen, and J.R. Turner. 2010. MLCK-dependent exchange and actin binding region-dependent anchoring of ZO-1 regulate tight junction barrier function. *Proc. Natl. Acad. Sci. USA.* 107:8237–8241. <https://doi.org/10.1073/pnas.0908869107>
- Yu, H.Y.E., and W.M. Bement. 2007. Control of local actin assembly by membrane fusion-dependent compartment mixing. *Nat. Cell Biol.* 9: 149–159. <https://doi.org/10.1038/ncb1527>
- Zhang, L., T. Ji, Q. Wang, K. Meng, R. Zhang, H. Yang, C. Liao, L. Ma, and J. Jiao. 2017. Calcium-sensing receptor stimulation in cultured glomerular podocytes induces TRPC6-dependent calcium entry and RhoA activation. *Cell. Physiol. Biochem.* 43:1777–1789. <https://doi.org/10.1159/000484064>
- Zhong, M., W. Wu, H. Kang, Z. Hong, S. Xiong, X. Gao, J. Rehman, Y.A. Komarova, and A.B. Malik. 2020. Alveolar stretch activation of endothelial Piezo1 protects adherens junctions and lung vascular barrier. *Am. J. Respir. Cell Mol. Biol.* 62:168–177. <https://doi.org/10.1165/rcmb.2019-0024OC>
- Zihni, C., C. Mills, K. Matter, and M.S. Balda. 2016. Tight junctions: From simple barriers to multifunctional molecular gates. *Nat. Rev. Mol. Cell Biol.* 17:564–580. <https://doi.org/10.1038/nrm.2016.80>

Supplemental material

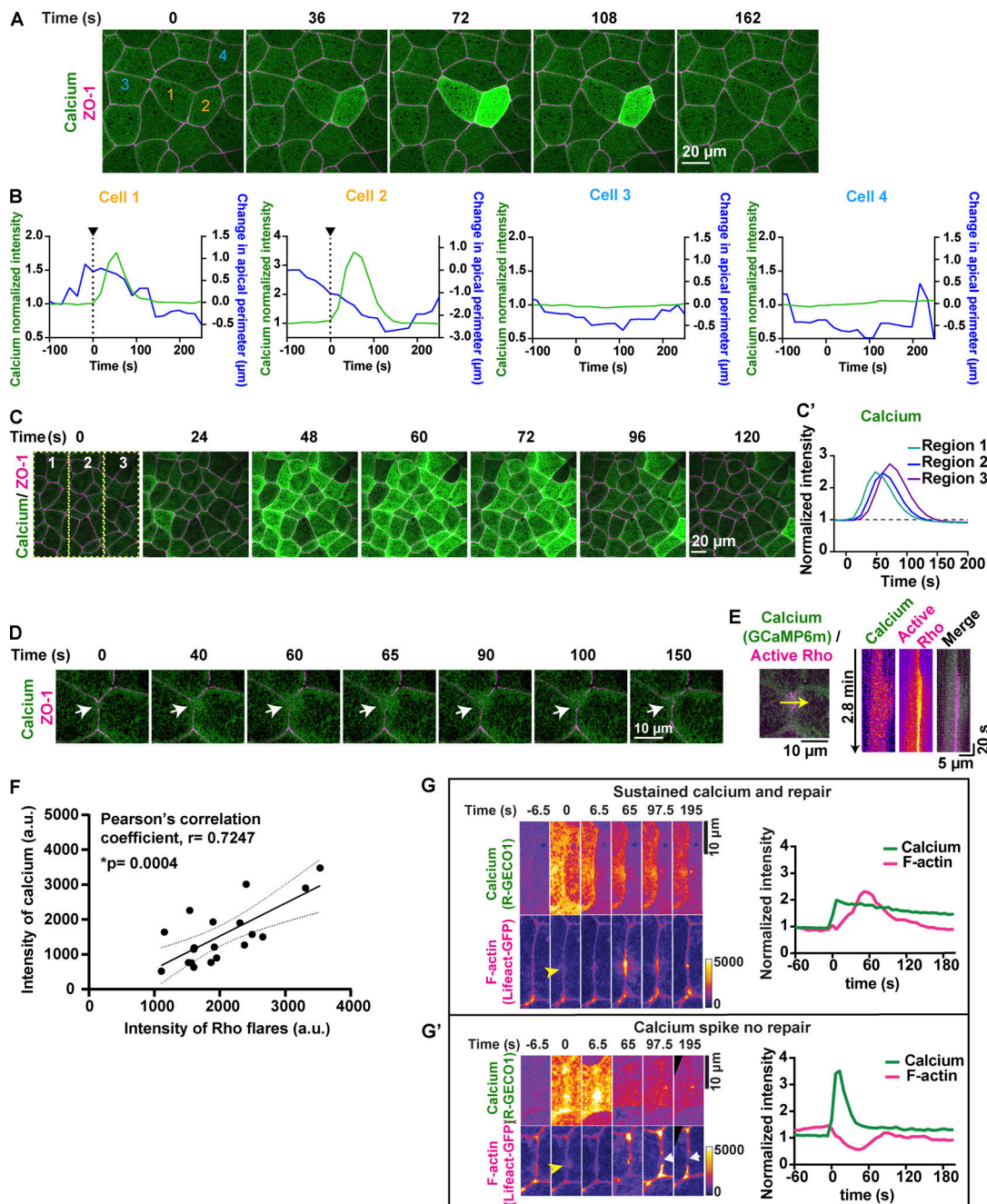


Figure S1. **Dynamics of calcium flashes and calcium waves in gastrula-stage *Xenopus* epithelia.** (A) Live imaging of calcium (GCaMP6m, green) and ZO-1 (BFP-ZO-1, magenta) in the animal cap epithelium of gastrula-stage *Xenopus* embryo. Calcium flash is short-lived and restricted to cell 1 and cell 2 (orange numbers). Time 0 s represents the start of the calcium flash. (B) Graphs showing change in cellular apical perimeter and calcium intensity in four different cells shown in A over time. Cells experiencing calcium flash (cells 1 and 2) decrease in apical perimeter compared with control cells (cells 3 and 4). (C) Live imaging of calcium (GCaMP6m, green) and ZO-1 (BFP-ZO-1, magenta) in the animal cap epithelium of gastrula-stage *Xenopus* embryos. Traveling calcium wave starts at time 0 s in region 1, propagates through regions 2 and 3, and subsides in ~120 s. (C') Graph showing the increase in calcium intensity over time in regions marked in the first frame of C. (D) Live imaging of calcium (GCaMP6m, green) and ZO-1 (BFP-ZO-1, magenta) showing a local calcium increase (white arrows) in cells expressing a reduced amount of GCaMP6m. Time 0 s represents the start of the calcium increase. (E) Left: Cell view of embryo expressing calcium probe (GCaMP6m, green) and active Rho probe (mCherry-2xrGBD, magenta). 5-pixel-wide yellow arrow indicates the region used to generate the kymograph. Right: Kymograph shows that cytosolic calcium increases locally at the site of the Rho flare. Individual images are shown using FIRE LUT. (F) Correlation plot between intensity of calcium and intensity of active RhoA at the maximum size of Rho flares shows a significant positive correlation, with a Pearson's correlation coefficient of $r = 0.7247$. Solid line represents the best-fit line, and the dotted lines represent the 95% confidence bands of the best-fit line. Significance calculated using two-tailed *t* test. $n = 19$ flares, 14 embryos, 11 experiments. (G and G') Time-lapse images (FIRE LUT) of calcium probe (R-GECO1) and F-actin probe (Lifeact-GFP) with sustained calcium increase (G) or a calcium spike (G') following laser-induced TJ injury. Yellow arrowhead indicates the site of junctional laser injury at time 0 s. (G) Montage and graph of normalized intensity shows successful activation of F-actin accumulation (magenta) and repair of laser-induced F-actin break following a local sustained calcium increase (green). (G') Montage and graph of normalized intensity shows failure to activate F-actin accumulation and lack of repair following a calcium spike that is not sustained over time. White arrows indicate the site of failed repair.

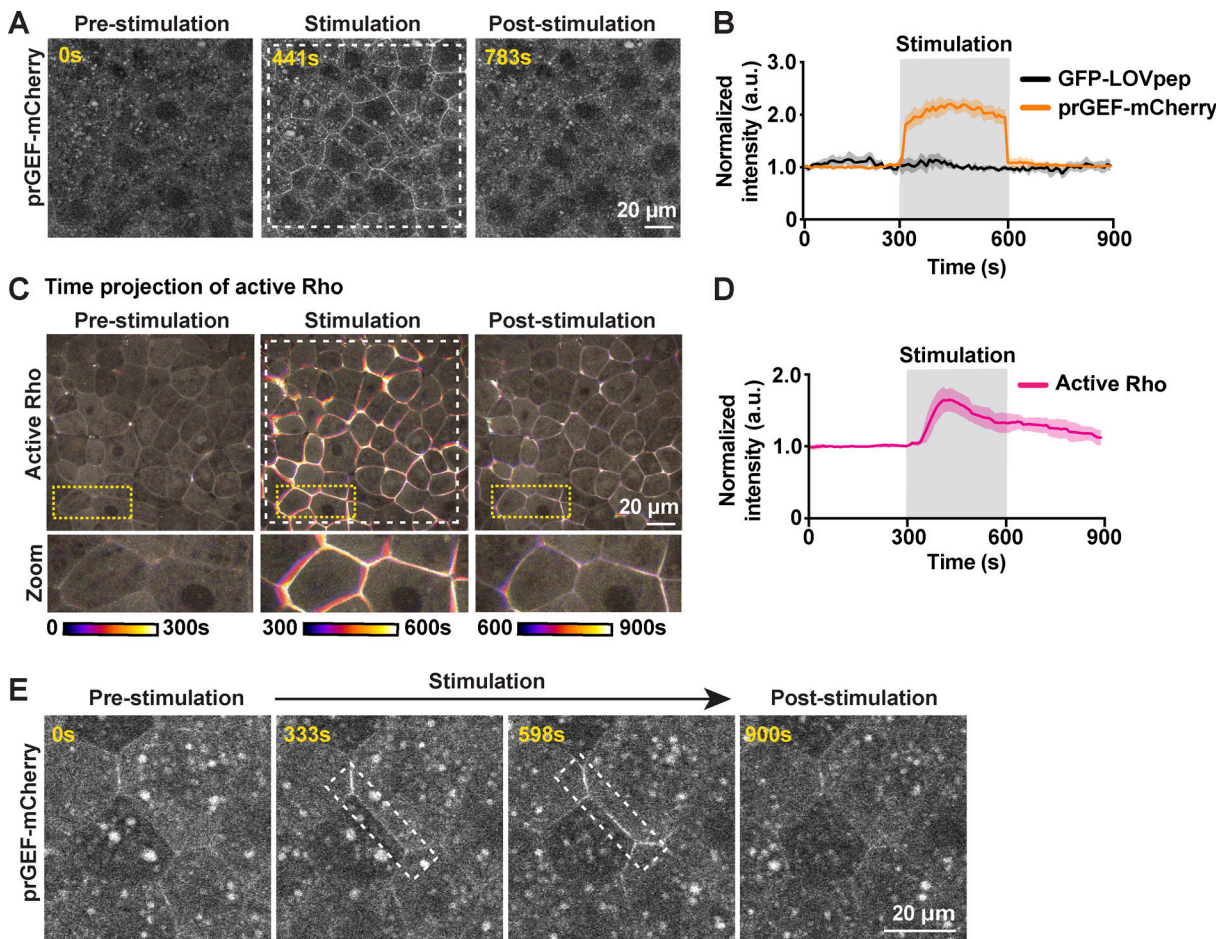


Figure S2. **Optogenetic stimulation of active RhoA induces whole-field tissue contraction.** (A) Whole-field 405-nm laser light stimulation (white dashed box) of an embryo expressing prGEF-mCherry (2xPDZ-mCherry-LARG(DH), gray) and GFP-LOVpep induces whole-field recruitment of prGEF-mCherry to junctions. (B) Quantification of experiments in A. Mean normalized intensity of prGEF-mCherry (2xPDZ-mCherry-LARG(DH)) and GFP-LOVpep upon whole-field 405-nm laser stimulation (gray shaded box, 300–600 s). Shaded regions represent SEM; GFP-LOVpep: $n = 9$ junctions, 3 embryos, 3 experiments; prGEF-mCherry: $n = 12$ junctions, 3 embryos, 3 experiments. (C) Time projection images of an embryo expressing active Rho probe (mCherry-2xrGBD, gray). Whole-field light stimulation (white dashed box) leads to increased active Rho at junctions and induces tissue contraction. Zoomed images of cells are indicated by yellow dashed boxes. (D) Quantification of experiments in C. Mean normalized intensity of active Rho probe (mCherry-2xrGBD) upon whole-field 405-nm laser stimulation (gray shaded box). Shaded regions represent SEM; $n = 30$ junction, 3 embryos, 3 experiments. (E) Site-specific light stimulation of a junction (white dashed box) expressing prGEF-mCherry (2xPDZ-mCherry-LARG(DH), gray) and GFP-LOVpep induces site-specific recruitment of prGEF-mCherry to the junction.

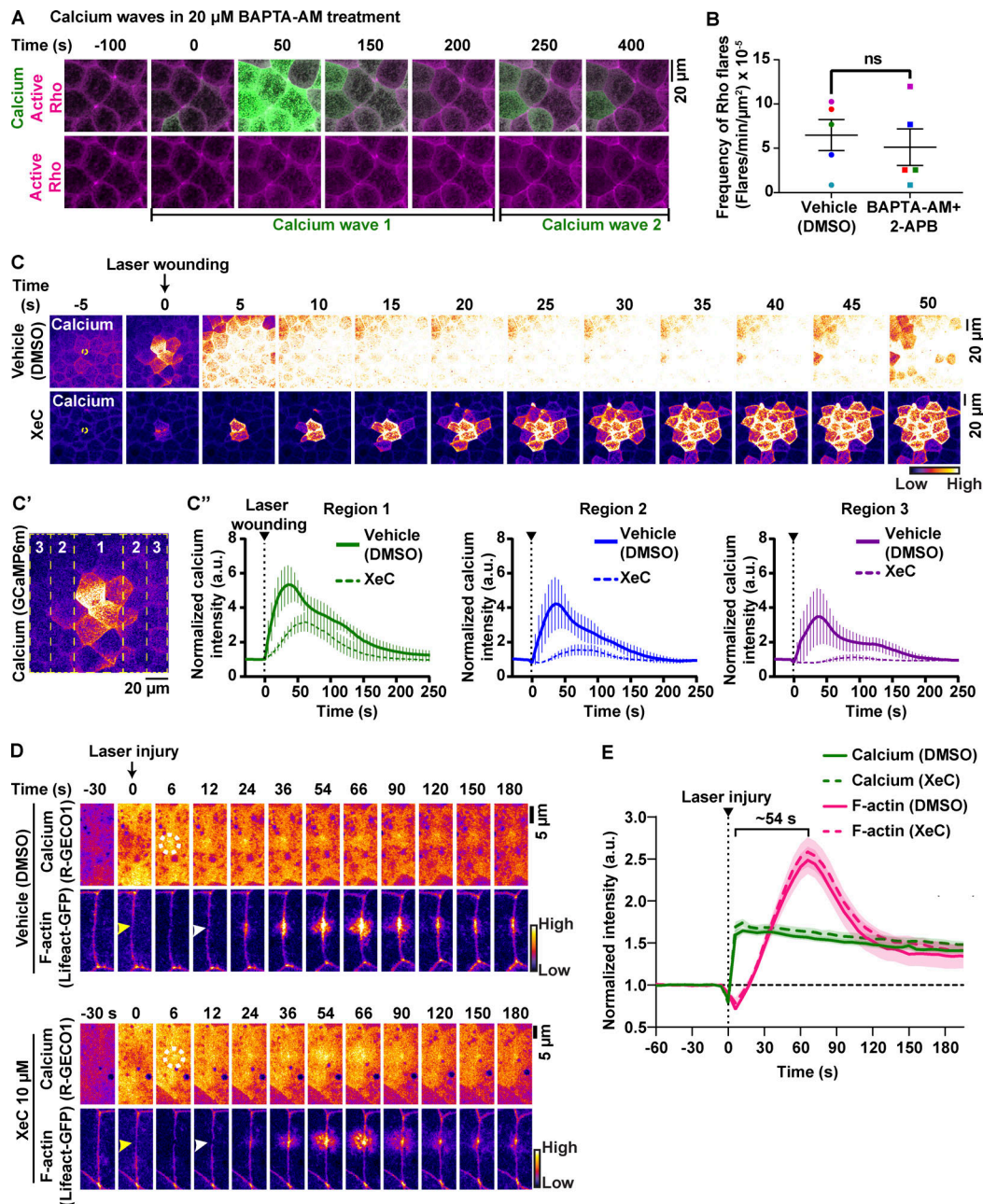


Figure S3. IP_3R -mediated calcium release is not required for calcium flashes and F-actin accumulation at TJ breaches. (A) Live imaging of calcium (GCaMP6m, green) and active Rho probe (mCherry-2xrGBD, magenta) in the animal cap epithelium of gastrula-stage *Xenopus* embryos treated with 20 μ M BAPTA-AM after vitelline removal. Montage shows recurring calcium waves within a span of ~ 500 s. The first calcium wave starts at time 0 s, and the second calcium wave starts at ~ 200 s. (B) Frequency of Rho flares in vehicle (DMSO) and calcium-chelated (BAPTA-AM + 2-APB) embryos. Frequencies from paired experiments are color matched. Error bars represent mean \pm SEM; significance calculated using paired two-tailed *t* test; *n* = 5 embryos, 5 experiments. (C–C'') Time-lapse images (FIRE LUT) of calcium probe (GCaMP6m) during laser wounding in embryos treated with vehicle (1% DMSO) or 10 μ M XeC (IP_3R blocker) for 1 h before imaging. (C) Montage shows that blocking IP_3R (XeC) reduces the intensity and spread of calcium from the site of laser-induced wounding to the neighboring cells compared with vehicle control. White dotted circle represents the site of laser wounding. Time 0 s represents the time of laser wounding. (C') Schematic shows the regions quantified over time in C'. (C'') Graphs show that the normalized intensity of calcium after laser wounding was reduced in XeC-treated embryos compared with vehicle controls in all three regions shown in C'. Error bars represent mean \pm SEM. Vehicle: *n* = 4 embryos, 2 experiments; XeC: *n* = 6 embryos, 2 experiments. (D) Time-lapse images (FIRE LUT) of calcium probe (R-GECO1) and F-actin probe (Lifeact-GFP) during laser-induced TJ injury in embryos treated with vehicle (1% DMSO) or 10 μ M XeC (IP_3R blocker) for 1 h before imaging. Local calcium increase (white dotted circles) precedes F-actin increase (white arrowheads) at the site of junctional laser injury (yellow arrowheads). Montage shows that the local calcium increase and F-actin accumulation at the site of TJ damage were comparable between vehicle- and XeC-treated embryos. Time 0 s represents time of junctional injury. (E) Quantification of experiments shown in D. Graph of mean normalized intensity shows that both intensity and time of calcium increase and F-actin accumulation following the laser injury in XeC (dotted lines) treatment were comparable to vehicle controls (solid lines). Shaded region represents SEM. Bracket represents the time interval between the peaks of calcium and F-actin. Vehicle: *n* = 31 flares, 14 embryos, 3 experiments; XeC: *n* = 27 flares, 12 embryos, 3 experiments.

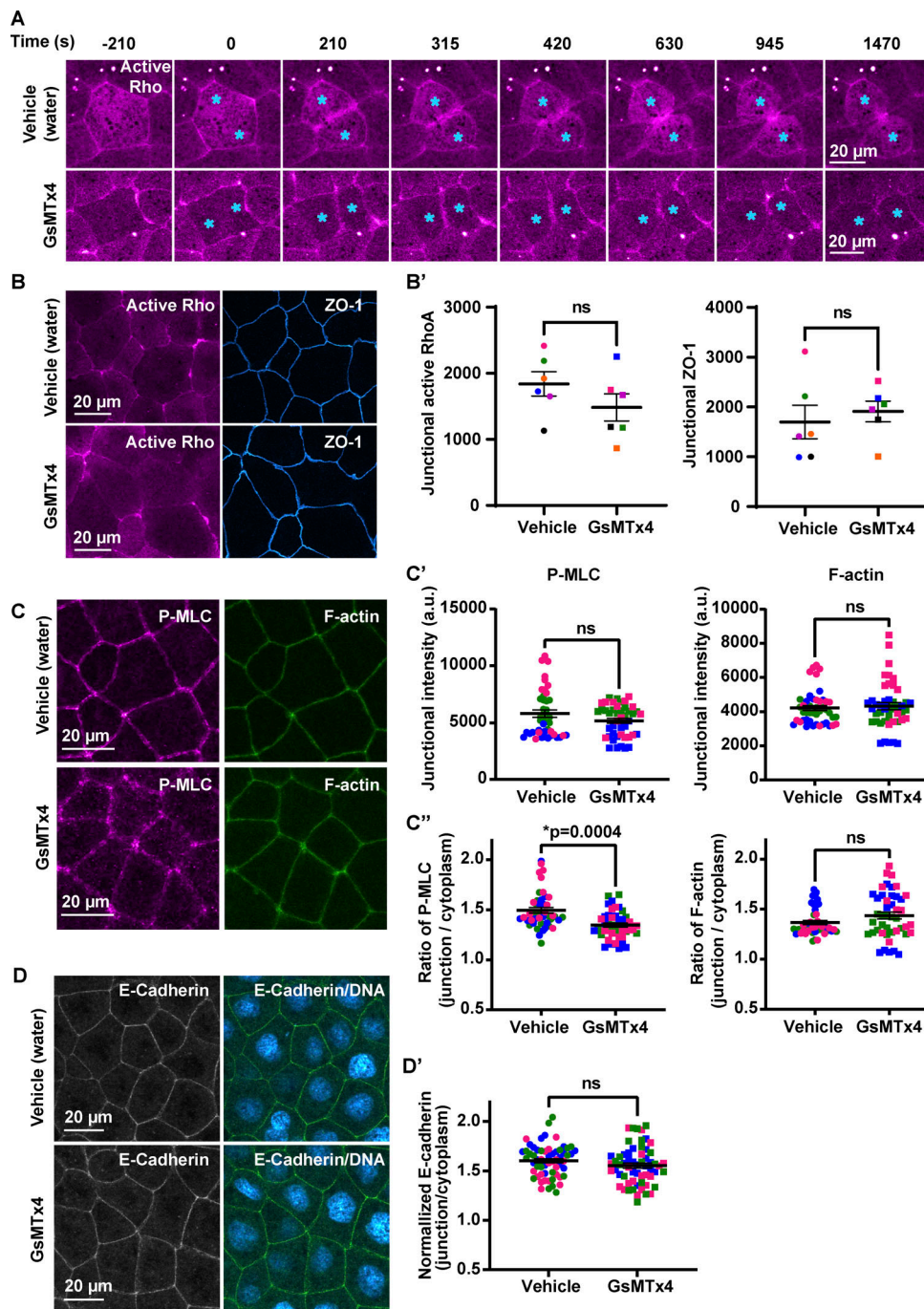


Figure S4. **Inhibition of MSCs does not significantly alter the overall morphology of cell-cell junctions.** **(A)** Live imaging of active Rho (mCherry-2xrGBD, magenta) in embryos treated with vehicle (water) or 12.5 μM GsMTx4 (MSC inhibitor). Montage shows that MSC inhibition does not affect Rho activity at the contractile ring, and cells complete cytokinesis successfully. Blue asterisk indicates dividing cells. Time 0 s represents the start of contractile ring formation. **(B and B')** Live imaging of active Rho (mCherry-2xrGBD, magenta) and ZO-1 (BFP-ZO-1, blue) in embryos treated with vehicle (water) or 12.5 μM GsMTx4. **(B)** Quantification shows that MSC inhibition does not significantly affect baseline junctional active RhoA or ZO-1 intensity at apical cell-cell junctions compared with vehicle controls. Junctional intensity of active Rho and ZO-1 from paired experiments are color matched. Error bars represent mean \pm SEM; significance calculated using Wilcoxon matched-pairs test; $n = 30$ junctions, 6 experiments. **(C-C')** Sum projection of fixed staining for P-MLC (anti-phosphomyosin light chain2, magenta) and F-actin (Alexa Fluor 647 phalloidin, green) in embryos treated with vehicle (water) or 12.5 μM GsMTx4. **(C')** Quantification shows that MSC inhibition does not significantly affect the junctional intensity of P-MLC and F-actin at cell-cell junctions compared with vehicle controls. **(C'')** MSC inhibition reduces the junction/cytoplasm ratio of P-MLC compared with vehicle but does not affect the junction/cytoplasm ratio for F-actin. Data points from paired experiments are color matched. Error bars represent mean \pm SEM; significance calculated using one-way ANOVA test; $n = 45$ junctions, 3 experiments. **(D)** Sum projection of fixed staining for adherens junctions (anti-E-Cadherin, green) and DNA (DAPI, cyan hot) in embryos treated with vehicle (water) or 12.5 μM GsMTx4. **(D')** Graph of the normalized intensity of E-Cadherin shows that MSC inhibition does not significantly affect the intensity of E-Cadherin at cell-cell junctions compared with vehicle controls. Data points from paired experiments are color matched. Error bars represent mean \pm SEM; significance calculated using Mann-Whitney U test; $n = 60$ junctions, 12 embryos, 3 experiments.

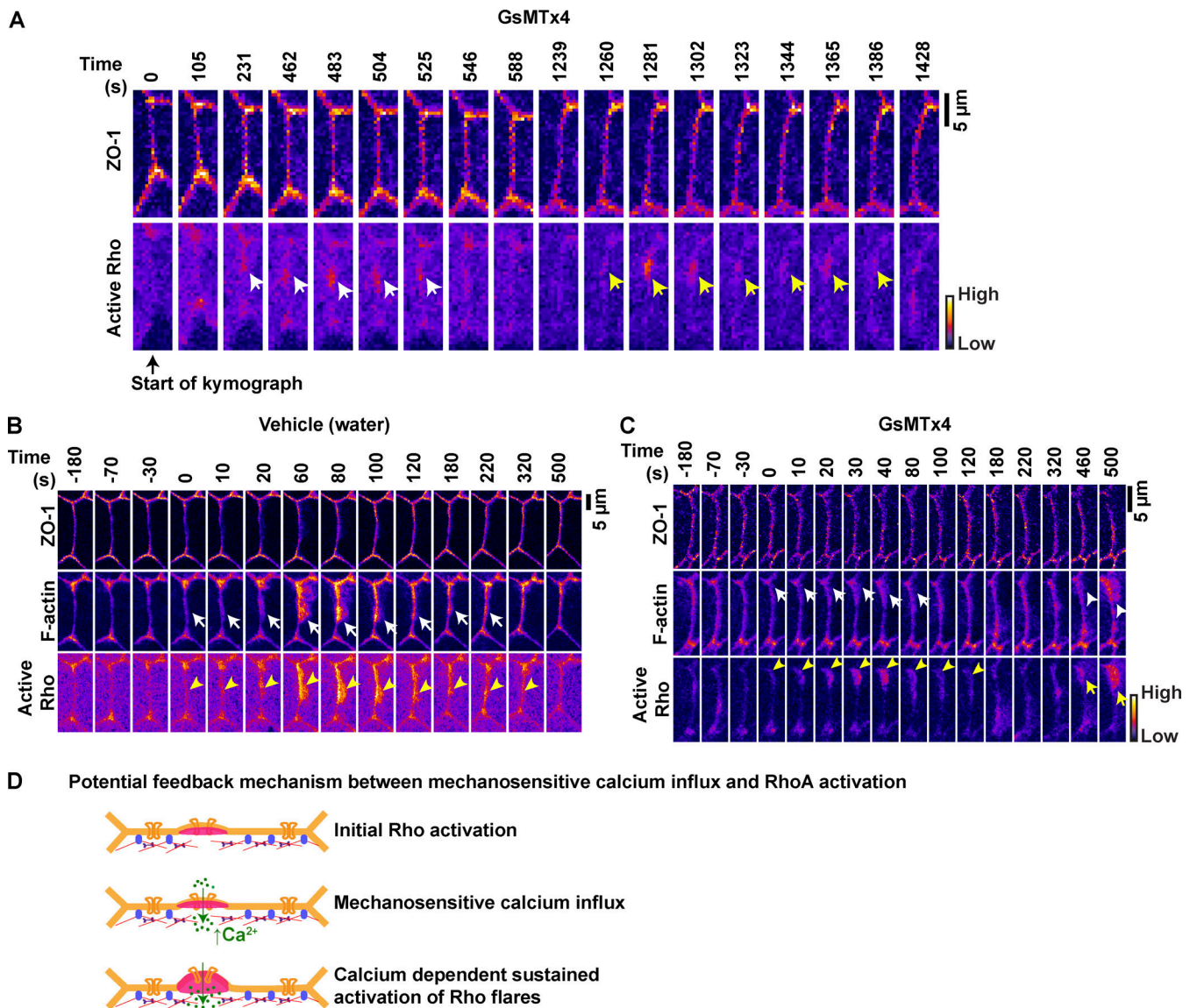


Figure S5. **Sustained Rho flares are required for robust F-actin accumulation and successful reinforcement of ZO-1.** (A) Montage of a representative junction used to construct kymograph in Fig. 7 G (FIRE LUT). Blocking MSCs with 12.5 μ M GsMTx4 causes repeated increases in active Rho at the site of reduced ZO-1 at time 231 s (first flare, white arrows) and 1,260 s (second flare, yellow arrows). Note that ZO-1 is partially reinforced following the first flare but breaks at the same site before activation of second flare. Time 0 s represents the start of kymograph in Fig. 7 G. (B and C) Time-lapse images (FIRE LUT) of ZO-1 (BFP-ZO-1), F-actin (Lifeact-GFP), and active Rho (mCherry-2xrGBD) in embryos treated with vehicle (water) or 12.5 μ M GsMTx4. Blocking MSCs with 12.5 μ M GsMTx4 causes reduced F-actin accumulation (C, white arrows) at the site of Rho flares (C, yellow arrowheads) compared with vehicle control in B. Note the robust F-actin accumulation scales (C, white arrowhead) with a higher-intensity repeating Rho flare (C, yellow arrow). Time 0 s represents the start of Rho flare. (D) Schematic of proposed positive feedback mechanism where initial activation of RhoA mediates membrane protrusion to promote MSC-dependent calcium influx, which in turn sustains the RhoA activation for robust actomyosin-mediated junction contraction at the site of ZO-1 repair.

Video 1. **Time-lapse confocal imaging of gastrula-stage *Xenopus* embryo showing that local calcium (BFP-C2, green) and active Rho (mCherry-2xrGBD, magenta) increase at the site of leaks (FluoZin-3, FIRE LUT).** Video illustrates that the FluoZin-3 increase precedes the local calcium increase. Time interval, 21 s; video frame rate, 5 fps. Related to Fig. 1, A and B.

Video 2. **Time-lapse confocal imaging of gastrula-stage *Xenopus* embryo shows the calcium (mNeon-C2, green) increases locally at sites of Rho flares (mCherry-2xrGBD, magenta) during cell shape changes.** Time interval, 10 s; video frame rate, 20 fps. Related to Fig. 1, C and D.

Video 3. **Time-lapse confocal imaging of gastrula-stage *Xenopus* embryo shows a naturally occurring calcium flash and calcium wave in a gastrula-stage *Xenopus* embryo expressing BFP-ZO-1 (magenta) and GCaMP6m (green).** Video shows that the calcium flash is restricted to two to three cells, whereas the calcium wave travels across the tissue. Time intervals, 18 s for calcium flash and 12 s for calcium wave; video frame rate, 2 fps. Related to [Fig. S1, A–D](#).

Video 4. **Time-lapse confocal imaging shows the dynamic activation of Rho flares (mCherry-2xrGBD, magenta) at the site of ZO-1 loss (BFP-ZO-1, cyan) and calcium flashes (GCaMP6m, green).** Time interval, 5 s; video frame rate, 20 fps. Related to [Fig. 2, C and D](#).

Video 5. **Time-lapse confocal imaging of gastrula-stage *Xenopus* embryo shows local and sustained increase in calcium (R-GECO1, green) and F-actin accumulation (Lifeact-GFP, magenta) at the site of a laser-induced TJ breach.** Note that the R-GECO1 intensity increases throughout the field of view only when 405-nm laser is turned on to induce laser injury. Time interval, 6.5 s; video frame rate, 10 fps. Related to [Fig. 2 E](#) and [Fig. S1 G](#).

Video 6. **Time-lapse confocal imaging of gastrula-stage *Xenopus* embryo showing whole-field optogenetic stimulation leading to prGEF-mCherry (2xPDZ-mCherry-LARG(DH), gray) recruitment and activation of Rho (mCherry-2xrGBD, gray).** First video illustrates whole-field recruitment of prGEF upon light stimulation, and second video illustrates whole-field activation of active Rho upon light stimulation. Time interval, 9 s; video frame rate, 20 fps. Related to [Fig. S2, A–D](#).

Video 7. **Time-lapse confocal imaging of gastrula-stage *Xenopus* embryo showing site-specific 405-nm laser light stimulation of junctions expressing optogenetic constructs along with active Rho probe (mCherry-2xrGBD, FIRE LUT) or calcium probe (Halo-C2, FIRE LUT).** First video shows increase of active Rho after site-specific light stimulation. Second video shows that local Rho activation is not sufficient to elicit a local calcium increase. Third video shows that upon laser injury of the same junction, there is an increase in local calcium at the site of the wound. White box indicates the region of stimulation. Time interval, 9 s; video frame rate, 10 fps. Related to [Fig. 3, C and D](#).

Video 8. **Time-lapse confocal imaging of gastrula-stage *Xenopus* embryo treated with 20 μ M BAPTA-AM + 100 μ M 2-APB for 1 h.** Video shows severe, long-lasting ZO-1 breaks (white arrows) and reduced activation of Rho flares (yellow arrowheads) in the absence of calcium flashes (GCaMP6m). All channels shown in FIRE LUT. Time interval, 5 s; video frame rate, 50 fps. Related to [Fig. 4 C](#).

Video 9. **Time-lapse confocal imaging of gastrula-stage *Xenopus* embryo illustrates the increased frequency of Rho flares (mCherry-2xrGBD, grayscale) in embryos treated with 12.5 μ M GsMTx4 (green arrowheads) compared with vehicle control (yellow arrows).** Dividing cells are marked by cyan asterisks. Time interval, 21 s; video frame rate, 20 fps. Related to [Fig. 7 C](#).

Video 10. **Time-lapse confocal imaging of gastrula-stage *Xenopus* embryo showing leaks (FluoZin-3, orange LUT) in embryos expressing BFP-ZO-1 (FIRE LUT) and active Rho probe (mCherry-2xrGBD, FIRE LUT).** First video shows the local increase of FluoZin-3 (white arrow) preceding the Rho flare (yellow arrowhead) at the site of ZO-1 decrease (white arrowhead) in vehicle (water) treated embryos. Second video shows repeated local increases of FluoZin-3 (green and white arrows) followed by short-duration Rho flare (yellow arrowhead) in embryos treated with 12.5 μ M GsMTx4. Time interval, 21 s; video frame rate, 5 fps. Related to [Fig. 7, D–E](#).